Redox Biology 41 (2021) 101926

Contents lists available at ScienceDirect

Redox Biology

journal homepage: www.elsevier.com/locate/redox

On-tissue polysulfide visualization by surface-enhanced Raman spectroscopy benefits patients with ovarian cancer to predict post-operative chemosensitivity

Kazufumi Honda [a,x,y,1], Takako Hishiki [b,1,2], Sohei Yamamoto [c,1], Takehiro Yamamoto [b], Nami Miura [a,y], Akiko Kubo [b], Mai Itoh [b], Wei-Yu Chen [d,e], Masashi Takano [f], Tomoyuki Yoshikawa [g], Takahiro Kasamatsu [h], Shinichiro Sonoda [i], Hirotoshi Yoshizawa [i], Seigo Nakamura [i], Yuichiro Itai [i], Megumi Shiota [i], Daisuke Koike [j], Masayuki Naya [i], Noriyo Hayakawa [b,2], Yoshiko Naito [b,2], Tomomi Matsuura [b,2], Keiko Iwaisako [k,l], Toshihiko Masui [k], Shinji Uemoto [k], Kengo Nagashima [m], Yoshinori Hashimoto [n], Tomohiro Sakuma [o], Osamu Matsubara [p], Wilber Huang [q], Tomoaki Ida [r], Takaaki Akaike [r], Yohei Masugi [s], Michiie Sakamoto [s], Tomoyasu Kato [t], Yoshinori Ino [u], Hiroshi Yoshida [v], Hitoshi Tsuda [w], Nobuyoshi Hiraoka [u,v], Yasuaki Kabe [b,x], Makoto Suematsu [b,*]

[a] Department of Biomarkers for Early Detection of Cancer, National Cancer Center Research Institute, Tokyo, Japan
[b] Department Biochemistry, Keio University School of Medicine, Tokyo, Japan
[c] Department of Diagnostic Pathology, Anjo Kosei Hospital, Aichi, Japan
[d] Department of Pathology, School of Medicine, College of Medicine, Taipei Medical University, Taipei, Taiwan
[e] Department of Pathology, Wan Fang Hospital, Taipei Medical University, Taipei, Taiwan
[f] Department of Obstetrics and Gynecology, National Defense Medical College, Saitama, Japan
[g] Department of Clinical Oncology, National Defense Medical College Hospital, Saitama, Japan
[h] Department of Obstetrics and Gynecology, Tokyo Metropolitan Bokutoh Hospital, Tokyo, Japan
[i] Frontier Core Technology Laboratories, R&D Management Headquarters, FUJIFILM Corporation, Ashigara-gun, Kanagawa, Japan
[j] FUJIFILM Business Expert Corporation, Ashigara-gun, Kanagawa, Japan
[k] Division of Hepato-Biliary-Pancreatic Surgery and Transplantation, Department of Surgery, Kyoto University, 54 Shogoin kawaracho, Sakyo, Kyoto, Japan
[l] Department of Medical Life Systems, Faculty of Life and Medical Sciences, Doshisha University, 1-3 Tatara Miyakodani, Kyotanabe city, Kyoto, Japan
[m] Research Center for Medical and Health Data Science, The Institute of Statistical Mathematics, Tokyo, Japan
[n] Scientific Imaging Scanner Department, System Division, Hamamatsu Photonics, Hamamatsu, Japan
[o] Bioscience Division, Mitsui Knowledge Industry Corporation, Ltd., Tokyo, Japan
[p] Department of Pathology, Hiratsuka Kyosai Hospital, The Cancer Institute, Kanagawa, Japan
[q] Abnova Corporation, Taipei, Taiwan
[r] Department of Environmental Medicine and Molecular Toxicology, Tohoku University Graduate School of Medicine, Sendai, Japan
[s] Department of Pathology, Keio University School of Medicine, Japan
[t] Division of Gynecology, National Cancer Center Hospital, Tokyo, Japan
[u] Division of Molecular Pathology, National Cancer Center Research Institute, Japan
[v] Department of Diagnostic Pathology, National Cancer Center Hospital, Tokyo, Japan
[w] Department of Basic Pathology, National Defense Medical College, Saitama, Japan
[x] AMED-CREST, Japan Agency for Medical Research and Development (AMED), Japan
[y] Department of Bioregulation, Graduate School of Medicine, Nippon Medical School, Japan

ARTICLE INFO

Keywords:
3-Mercaptopyruvate sulfotransferase
Cancer stroma

ABSTRACT

Chemosensitivity to cisplatin derivatives varies among individual patients with intractable malignancies including ovarian cancer, while how to unlock the resistance remain unknown. Ovarian cancer tissues were

* Corresponding author. Department of Biochemistry, Keio University School of Medicine, 35 Shinanomachi, Shinjuku-ku, Tokyo 160-8582, Japan.
E-mail address: gasbiology@keio.jp (M. Suematsu).
[1] K.H., T.H., and S.Y. are equally contributed as first authors.
[2] T.H., N.H, Y.N., and T.M. are engaged in Clinical and Translational Research Center, Keio University School of Medicine.

https://doi.org/10.1016/j.redox.2021.101926
Received 26 January 2021; Received in revised form 23 February 2021; Accepted 26 February 2021
Available online 2 March 2021

Ambroxol
Imaging metabolomics

collected the debulking surgery in discovery- (n = 135) and validation- (n = 47) cohorts, to be analyzed with high-throughput automated immunohistochemistry which identified cystathionine γ-lyase (CSE) as an independent marker distinguishing non-responders from responders to post-operative platinum-based chemotherapy. We aimed to identify CSE-derived metabolites responsible for chemoresistant mechanisms: gold-nanoparticle (AuN)-based surface-enhanced Raman spectroscopy (SERS) was used to enhance electromagnetic fields which enabled to visualize multiple sulfur-containing metabolites through detecting scattering light from Au–S vibration two-dimensionally. Clear cell carcinoma (CCC) who turned out less sensitive to cisplatin than serous adenocarcinoma was classified into two groups by the intensities of SERS intensities at 480 cm^{-1}; patients with greater intensities displayed the shorter overall survival after the debulking surgery. The SERS signals were eliminated by topically applied monobromobimane that breaks sulfane-sulfur bonds of polysulfides to result in formation of sulfodibimane which was detected at 580 cm^{-1}, manifesting the presence of polysulfides in cancer tissues. CCC-derived cancer cell lines in culture were resistant against cisplatin, but treatment with ambroxol, an expectorant degrading polysulfides, renders the cells CDDP-susceptible. Co-administration of ambroxol with cisplatin significantly suppressed growth of cancer xenografts in nude mice. Furthermore, polysulfides, but neither glutathione nor hypotaurine, attenuated cisplatin-induced disturbance of DNA supercoiling. Polysulfide detection by on-tissue SERS thus enables to predict prognosis of cisplatin-based chemotherapy. The current findings suggest polysulfide degradation as a stratagem unlocking cisplatin chemoresistance.

1. Introduction

Platinum-based chemotherapy with agents such as cisplatin (CDDP) offers survival benefits in patients with ovarian cancer who undergo primary debulking surgery [1]. However, the outcomes of patients without efficacy from the chemotherapy after debulking surgery are significantly worse than those of responsive patients. If mechanisms of the resistance against platinum-based chemotherapy for ovarian cancer can be identified, combination therapies with inhibition of the mechanisms for resistance against platinum-based chemotherapy would potentially increase the survival benefits for advanced-stage patients treated by debulking surgery for ovarian cancer. This study aimed to identify biomarkers predictive of patients with resistance to platinum-based chemotherapy which are determined by analyzing tissues of ovarian carcinoma collected in occasion of the surgery.

To that effect, we have carried out high throughput screening of tissue microarrays (TMAs) made from the resected tissues of ovarian carcinoma which had undergone the platinum-based chemotherapy after the debulking surgery for stage-III/IV ovarian cancer after debulking surgery. The analyses allowed us to identify significant overexpression of cystathionine γ-lyase (CSE; EC 4.4.1.1) in patients with stage-III/IV ovarian cancer who showed resistance to platinum-based chemotherapy after debulking surgery. CSE is an enzyme that catalyzes conversion of cystathionine to cysteine that serves as a substrate for multiple terminal products including reduced glutathione (GSH) and hypotaurine (HT) and reactive sulfur species (RSS) [2–8]. RSS include hydrogen sulfide (H_2S) and hydropolysulfides [4–8], metabolites with potent reducing actions. We have herein revealed that L-SERS serves as a potentially useful method for on-tissue visualization of endogenous polysulfides in post-operative ovarian cancer tissues to predict chemosensitivity and overall survival. Furthermore, chemoresistant mechanisms appear to involve the potent action of polysulfides to interfere with DNA intercalation of cisplatin as a nucleophilic reagent.

2. Materials and methods

2.1. Patients and tissue samples

This study was performed with the approval from the Internal Review Boards (IRBs) on ethical issues of the NDMC (Tokorozawa, Japan) and NCC (Tokyo, Japan) under written form of informed consents. The patient-derived tissue slices of ovarian cancer were obtained from the NCC Biobank and were prepared and mounted in NCC and transferred to the Keio University School of Medicine for SERS imaging and imaging mass spectrometry. This study was performed under the approval of the Internal Review Board (IRB) of National Cancer Center on ethical issues (2009-053, 2010-077, 2010-221 and 2017-340), and that of IRBs (20130398) of Keio University School of Medicine (Tokyo, Japan) and FUJIFILM Corporation (Kanagawa, Japan).

We collected formalin-fixed paraffin-embedded (FFPE) surgical tissue specimens from 2 hospitals (NDMC and NCC), from a total of 186 patients who underwent surgical resection of stage III or IV ovarian cancer. All patients were treated with postsurgical platinum-based combination chemotherapy, but none had undergone preoperative neoadjuvant chemo- or radiotherapy. The histological type of tumor was classified according to the World Health Organization criteria. Histological grading, with reference to the grading systems proposed by previous studies [9,10], was performed as described previously [11]. The International Federation of Gynecology and Obstetrics system was used for staging. Clinical response to chemotherapy was evaluated using ultrasonography or computed tomography and classified into complete response (CR), partial response (PR), stable disease (SD), and progressive disease (PD) according to RECIST version 1.1 guidelines [12].

Tissue slices for imaging metabolomics by using L-SERS imaging and imaging MS were derived from deeply frozen cancer and noncancerous tissue specimens from the patients and were obtained from the National Cancer Center Biobank. These tissue samples including ovarian cancers were collected after receiving written informed consent from the patients. Board-certified pathologists who have national licence then macroscopically confirmed the presence of tumor cells in all tissue samples. A fresh noncancerous ovarian tissue was obtained from a patient with colon cancer, who was diagnosed with uterine leiomyoma and underwent hysterectomy and adnexectomy. Information of histological types and the values of overall survival (OS) were blinded to those who examined imaging metabolomics using L-SERS and imaging MS.

2.2. Cohorts in NDMC and NCC for ovarian cancer

The discovery cohort-NDMC included 139 patients who had undergone surgery followed by platinum-based chemotherapy for stage III or IV primary ovarian cancer at the Department of Obstetrics and Gynecology, NDMC, between 1987 and 2005 (Table 1). Chemotherapeutic regimens were as follows: cyclophosphamide (CPA), doxorubicin (DXR), and CDDP in 80 patients; paclitaxel (PTX) and carboplatin (CBDCA) in 28 patients; irinotecan (CPT-11) and CDDP in 10 patients; etoposide (VP-16) and CDDP in 6 patients; docetaxel (DOC) and CBDCA in 6 patients; CPT-11 and CDDP in 5 patients; CPT-11 and CBDCA in 1 patient; and CPA and CDDP in 1 patient. The validation cohort-NCC included 47 patients with stage III or IV primary ovarian cancer who had undergone surgery at the Gynecology Division of the NCC hospital between 1983 and 2001 (Table 1).

Table 1
Clinicopathological characteristics of patients in 2 independent cohorts.

Cohort	Discovery cohort-NDMC[a]	Validation cohort-NCC
	($N = 139$)[f]	($N = 47$)
Age		
56<	79	22
55≥	60	25
FIGO stage[b]		
III	104	37
IV	35	10
Histological type[c]		
Serous	89	32
Clear cell	27	8
Endometrioid	10	3
Mucinous	13	3
unknown or unclassified	0	1
Histological grade[d]		
1 or 2	42	NA[a]
3	97	NA
Residual tumor after surgery		
0–2 cm	62	25
>2 cm	77	18
Unkown	0	4
Response to chemotherapy[e]		
Responders (CR/PR)	44	11
Non-responders (SD/PD)	33	3
unknown	0	4

[a] Abbreviations: NDMC, National Defense Medical College Hospital; NCC, National Cancer Center Hospital; NA, not available; CR, Complete response; PR, partial response; SD, stable disease; PR, progressive disease.
[b] According to the International Federation of Gynecology and Obsterics (FIGO) staging system.
[c] According to the World Health Organization (WHO) criteria.
[d] According to Silverberg grading.
[e] According to evolution with Response Evaluation Criteria in Solid Tumors (RESIST) guideline.
[f] Maximum numbers of first screening on the tissue microarrays (TMAs) using antibody library. The part of antibodies could not screen the maximum numbers, due to include the cases which cannot be well evaluated by TMAs.

2.3. Antibodies for TMA and fluorescence immunohistochemistry

A total of 1,012 mouse monoclonal antibodies were generated at the Abnova facility (Taipei, Taiwan; Supplementary Tab. S1). The specificity of all antibodies to corresponding antigens was verified using immunoblotting and IHC. All data are available at http://www.abnova.com. FFPE specimen cores (2.0 mm in diameter) were obtained from host blocks in areas used for histological grading and transferred to recipient blocks by using a Tissue Microarrayer (Beecher Instrument, Silver Spring, MD). TMA blocks were cut into 4-μm-thick sections. Double-color immunofluorescence staining was performed using an automatic immunostaining system (Ventana Discovery; Ventana, Tucson, AZ). Anti-human cytokeratin 19 rabbit polyclonal antibody (Abnova) and the 1,012 mouse monoclonal antibodies were used as primary antibodies. Anti-rabbit IgG Alexa 594 (Invitrogen, Carlsbad, CA) and anti-mouse IgG Alexa 488 (Invitrogen) antibodies were used as secondary antibodies. The concentrations of monoclonal antibodies used for immunofluorescence microscopy are shown in Supplementary Tab. S1. The schematic diagram with data processing flow chart were shown in Supplementary Fig. S1.

Stained TMAs were scanned using the Virtual Slide Scanner (NanoZoomer 2.0-HT; Hamamatsu Photonics, Hamamatsu, Japan) equipped with a triple fluorescence filter. Virtual microscopic images were constructed using scanner software (NanoZoomer Digital Pathology Virtual Slide Viewer version 2.2; Hamamatsu Photonics). A black rectangular array template, onto which the white circles of spot templates were allocated at even intervals, was matched to the virtual image of the TMA; next, the position of each spot template on the array template was adjusted to each spot image by using correlation coefficients between spot images and corresponding spot template images [13].

2.4. Antibody screening

The antibody library was screened using TMAs containing at least 50 surgical specimens that were resected at the NDMC Hospital. Antibodies showing positive immunoreactivities as candidate biomarkers were selected from the antibody library by using two criteria: First, antibodies with significant prognostic impact on OS according to the expression levels of antigens ($p < 0.05$). and secondly, antibodies for which distinct antigen expression could be observed in cancer cells on virtual immunofluorescent pathology images. Prognostic significances of antibodies selected using these two criteria were again confirmed by TMAs from 139 patients with ovarian cancer who had undergone platinum-based chemotherapy after debulking surgery at NDMC (discovery cohort-NDMC; Table 1). The expression patterns of antibodies associated with prognostic significances ($p < 0.05$) for OS were selected after the first screening. Next, to validate the clinical impact of the predictive biomarker in ovarian cancer, we prepared other TMAs from patients with ovarian cancer who had undergone platinum-based chemotherapy after debulking surgery at the National Cancer Center Hospital (Table 1).

2.5. Statistical analysis for clinical data

OS was defined as the time from surgery to either last follow-up or death. Survival curves were plotted using the Kaplan–Meier method, and the significance of differences was analyzed using the stratified log-rank test. The chi-squared test, Fisher's LSD test, Student's *t*-test, and Cox proportional hazards regression modelling were performed using the StatFlex statistics package (version 5.0; Atiteck, Osaka, Japan) or tools provided by the R-Project (http://www.r-project.org/) [16–19]. Differences in the wave number-specific signals between cancer cell regions and cancer stromal regions were determined statistically by using Benjamini–Hochberg's false discovery rate analyses for multiple comparison [14]. Differences in variation of the SERS signals between clear cell carcinoma (CCC) and serous adenocarcinoma (SAC) were examined by Kolmogorov-Smirnov test.

2.6. GNF-SERS imaging with high-speed confocal laser scanning microcopy

The fabrication of GNF substrates followed our previous method [4] and has been described in the section of a schematic diagram of line-scanning L-SERS imaging. As reported in the previous study [4], the substrate was named gold nanofève (GNF) after the shape of Au nanoparticles that generate many electromagnetic hotspots as SERS excitation sources and enable large-area visualization of molecular vibration fingerprints of metabolites in tissue slices with sufficient sensitivity and uniformity. The optical transparency of the GNF substrate enabled the visualization of the Raman signals by using an inverted-type laser confocal microscope. The inverted-type Raman microscopic system used in this study (Ramanforce; Nanophoton Corporation., Suita, Osaka) was equipped with ×50 (NA = 0.65) objective lens that provided optimal conditions such that the SERS signals could be maximally enhanced. The design of the optical system and positional matching with the data of pathological annotation are described in Supplementary Fig. S2. The polychromatic unit enabled to achieve SERS spectra under different conditions of diffraction grating with 300 grooves mm^{-1}. The time for laser scanning was minimized by routinely acquiring SERS images at 300 grooves mm^{-1}, unless otherwise mentioned. Under the routine conditions of the ×50 objective lens, a horizontally lining laser beam at a width of 186 μm (=400 pixels/line) was scanned vertically, and the signals yielded from 50 pixels were binned to output the signals per 8 pixels/line. Finally, a series of the laser scanning stripe images was tiled to cover the entire microscopic fields. All spectral data were stored at individual 50-binned pixels into the computer storage (Supplementary

Fig. S2). Under these circumstances, the system allowed spatial resolution of 23.3 μm/pixel, unless otherwise mentioned. The sensitivity and frequency of the microscope system were calibrated using the 520 cm^{-1} Raman shift of silicon phonon mode before SERS measurements were performed. The back-ground noise of SERS signals was subtracted from the recorded spectra by using the weighted mean fitting with Lanczos second function [4,15]. The resolutions of wavenumbers were about 2 cm^{-1}, when the grating of 300 grooves mm^{-1} was used for SERS measurements, respectively.

Metabolites in the air-dried tissue sections prepared from frozen blocks of ovarian carcinoma stored in NCC Biobank were visualized by mounting 5-μm-thick tissue sections on GNF substrates and placing in the vacuum dry chamber. Before SERS imaging experiments, we used a microneedle to insert 3 micro-scratches at the outer regions of the tissue slices on the surface of the SERS substrate; the scratches were identified by light microscopy as well as SERS imaging and were thus useful to match spatial orientation between SERS images and H-E staining to analyze differences in region-specific SERS spectra between cancer cell and cancer stromal regions. To achieve a quality of SERS images with greater signal-noise ratios, we accumulated SERS signals at the central peak wave number of ±10 cm^{-1}.

To prove the presence of polysulfides in the tissue slices on SERS substrates, we prepared 5 mM monobromobimane (mBBr), a potent electrophilic reagent cleaving sulfane sulfur bonds of polysulfides which was dissolved in acetonitrile, and 1.0 μl of the mBBr solution was applied on the slices. Since mBBr reacts with polysulfides to generate sulfide dibimane (SDB), the combined data showing decreases in polysulfide signals at 480 cm^{-1} and increases in SDB signals at 452 cm^{-1} and 583 cm^{-1} serve as a hallmark to show endogenous polysulfides in the tissue samples as shown in Results.

2.7. Pathological annotation of cancer cell nests and stroma

We further investigated the spatial relationship between L-SERS imaging and hematixylin-eosin (H-E staining) which were acquired after SERS imaging and were annotated to identify cancer cell nests and the surrounding stromal regions by a board-certified pathologist (Supplementary Fig. S2). Immediately after the SERS images of tissue sections were recorded, the same sections were stained with H-E. The microscopic images of H-E-stained tissue sections mounted on optically transparent GNF substrates were directly imported as digital photo files by using NanoZoomer v.2.0-HT (Hamamatsu Photonics, Hamamatsu, Japan). Cancer cells were annotated by manually tracing cancer cell nests by certified professional pathologists at the magnification of 10× or 20× by using a 27-inch monitor and NDP view2 software (Hamamatsu Photonics, Hamamatsu City, Shizuoka), while carefully excluding non-cancer cells and structures, including any extracellular materials. We also annotated non-cancerous stroma within the cancer tissues by using the identical method described above to trace non-cancerous stromal regions instead of tracing cancer cell nests. The non-cancerous stroma is defined as stromal regions that do not contain any cancer cells within cancer tissues. If candidate regions of the stroma in cancer tissues include cancer cells that disturb the annotation of the stroma, such regions were excluded from the annotation. Cancer tissues are defined as an area surrounded by the borderline of the invasive margin of cancer cells.

2.8. MALDI imaging mass spectrometry

In separate sets of experiments, we conducted imaging MS (IMS) according to our previous methods [4,16]. Serial sections prepared for SERS imaging were used for AP-MALDI-IMS. In brief, as a matrix, 5 mg/ml 9-aminoacridine (Merck Schuchardt, Hohenbrunn, Germany) in 80% ethanol solution was sprayed over 5-μm-thick frozen tissue slices of ovarian cancer that were thaw-mounted on ITO-coated glass slides (Matsunami Glass IND., LTD., Osaka, Japan). AP-MALDI-IT-TOF mass spectrometer (Shimadzu Corp., Kyoto) enabled the application of pin-point laser beams at 35-μm intervals. The mass peaks of metabolites collected from tissue sections were identified by comparing MS/MS fragment patterns with those collected from standard reagents. The specific mass peaks of cysteine, glutathione, and cysteine persulfide, and glutathione persulfide and their sulfonated end products were determined and visualized by grating the m/z values of their specific mass fragments within a range of $m/z \pm 0.01$ to minimize noise signals [4,16]. The heterogeneity of mass signals among different tissue slices was minimized by taking the ratio imaging after the measurements [4,16]; Under conditions of atmospheric pressure MALDI, cysteine persulfide and glutathione persulfide were readily oxidized to cysteine *S*-sulfonate and glutathione *S*-sulfonate, respectively [4]. The amounts of these persulfides were indirectly compared on tissue slices by obtaining the ratio images of their oxidative terminal end products versus those of each parent thiols, namely, Cys-SSO_3^-/Cys-SO_3^- or $GSSO_3^-$/GSO_3^-, according to our previous methods [4,16].

2.9. Cell culture and chemicals used to examine viability of cultured cell lines

Ovarian cancer cell lines used in this study (OVISAHO, OVTOKO, KURAMOCHI, RMUG-S, TYK-nu Cp-r, TYK-nu, ES-2, and OVACAR-3) were obtained from the American Type Culture Collection (Manassa, VA) or the Japan Collection of Research Bioresources (Osaka, Japan) and cultured as recommended by the suppliers. CDDP (Randa) was purchased from Nippon Kayaku (Tokyo, Japan).

OVISE and OVTOKO cells which are derived from ovarian clear cell carcinoma, and OVCAR-3 cells, mimicking serous adenocarcinoma, were purchased from ATCC. These cells were plated on 96-well white plates (Thermo Fisher) at 3×10^3 cells $well^{-1}$. Attached cells (50–60% confluency) were treated with 25 μM ambroxol hydrochloride (A9797, Sigma) and CDDP (*cis*-diammineplatinum (II) dichloride; SIGMA, P4394) for 48 h. Apoptosis was assessed using the Realtime-Glo Annexin V apoptosis assay kit (Promega, JA1000), according to manufacturer's instructions. In brief, reagents for detection were added 4 h before measurement. Luminescence was determined using the SpectraMAX L microplate reader (Molecular Devices, Sunnyvale, CA). Western blot analyses were performed to detect the protein expression of the enzymes involving serine/glycine cleavage systems and trans-sulfuration pathway, according to our methods described in Supplementary Information [4,16,17]. Uncropped blotting data were shown in Supplementary Information. Stable knockdown was performed using the Mission short hairpin (sh)RNA lentiviral transduction system (Sigma-Aldrich). Three different constructs of shRNA targeting CSE: 5′-CCGGGCACC TCATTATCTTTCATAACTCGAGTTATGAAAGATAATGAGGT GCTTTTT G-3′: TRCN0000078263; 5′-CCGGCCTTCATAATAGACTTCGTTTCTCG AGAAACGAAGTCTATTATGAAGGTTTTTG-3′: TRCN0000078264; 5′-C CGGCCA CTAGGAATTGCCTTGAAACTCGAGTTTCAAGGCAATTCCTAG TGGTTTTTG-3′: TRCN0000078266; and an empty vector control construct were infected into OVISE cells. Hexadimethrine bromide (Sigma-Aldrich) at a concentration of 8 μg/ml was used to enhance the infection efficiency. Cells were selected using 2 μg/ml of puromycin (Invitrogen). The construct with pcDNA 3.1 was used for overexpression.

2.10. SDB measurements

Intracellular levels of reactive sulfur species (RSS) in OVISE, OVTOKO and OVCAR3 were assessed using monobromobimane (mBBr). Cells were washed with 5% mannitol twice, and then plunged into 500 μl methanol containing 100 nM of D-camphor-10-sulfonic Acid (CSA) as the internal standard. Cell extracts were thoroughly mixed with 500 μl deionized water and 1 ml chloroform, followed by centrifuging at 12,000 *g* for 15 min at 4°C. The upper aqueous phase was filtered through a centrifugal filter (Ultrafree-MC, 5-kDa cutoff; Human

Metabolome Technologies, Tsuruoka, Japan) to remove protein precipitates. After the lyophilization of filtrates, the precipitates were dissolved in 50 μl deionized water. The samples were incubated with 2 mM mBBr on ice for 5 min. Levels of mBBr derivatives were determined by LCMS-8030plus (Shimadzu, Kyoto, Japan). Obtained data were normalized by cellular protein concentrations [4,7,16]. When necessary, GSH, GSSG, hypotaurine were determined by LC-MS according to our previous method [4].

2.11. Effects of ambroxol on CDDP sensitivity to xenografting OVISE cells in nude mice

Effects of ambroxol on CDDP-induced regression of tumour growth in vivo were examined in xenograft experiments [16,17]. Briefly, BALB/c female nude mice at 6 weeks of age were purchased from CLEA Japan, Inc. (Tokyo, Japan). Human ovarian clear cell carcinoma-derived OVISE cells were injected subcutaneously at 2 x 10^6 cells into the dorsum of the mice. At the 10th day after transplantation, 25 mice were randomized into 3 groups: Groups A, B and C were the control treated with saline, with saline + CDDP at 10 mg/kg, and with ambroxol at 100 mg/kg + CDDP at 10 mg/kg, respectively. The intraperitoneal administration of saline or ambroxol followed the CDDP injection was given every day. The body weight and tumor sizes were measured every 2 days. The tumor volumes were calculated by the following formula: Volume (mm^3) = (length x width x width)/2. Alterations in the ratio of tumor volumes versus the baseline tumour volumes of individual mice measured at 10 days after the cell transplantation were monitored with body weights. Study protocols of the xenograft experiments were approved by Institutional Review Boards of Keio University for Animal Ethics Committee which follows declaration of Helsinki.

2.12. Generation of CSE knockout stable cell lines

CSE-deficient OVISE cell line was generated using the CRISPR/Cas9 recombination system [18]. The sgRNA targeting human CSE (CTTCCAACATTTCGCCACGC) was cloned into pLentiCRISPR v2 vector (purchased from Addgene, #52961). Lentivirus for sgRNA against human CSE was infected OVISE cells. Following puromycin selection (1 μg/ml for 2 weeks), CSE-deficient OVISE cells (sgCSE) were obtained. The empty vector pLentiCRISPR v2 was used as a control (sgControl). The mixed cell populations were used for the experiments to detect protein polysulfides according to the method described in the following section.

2.13. Protein persulfide detection in OVISE cell lysates

Protein persulfides were assayed to compare differences among cultured cell lines such as OVISE, OVTOKO and OVCAR3 according to the dimedone-based method described elsewhere [19,20]. Briefly, one of these cells were grown to 80%–90% confluency in a 100 mm dish. After washing with PBS twice, cells were scraped and lysed with 1 ml ice-cold HEN lysis buffer (50 mM HEPES, 1 mM EDTA, 0.1 mM neocuproine (SIGMA, N1501), 100 μM deferoxamine (abcam, ab120717), and 1% protease inhibitor; pH7.4) containing 5 mM 4-chloro-7-nitrobenzofurazan (NBF–Cl)(SIGMA, 163260) and incubated at 37°C for 60min, protected from light. Labeled lysates were precipitated with methanol/chloroform (Sample: methanol: chloroform = 4:4:1(v/v/v)) with centrifugation at 14000×*g* for 15 min at 4°C. Protein layers were collected, and then dissolved in 200 μM HEPES (50 mM, pH 7.4) containing 2% SDS. After determination of protein concentration, 50 μg NBF–Cl-labeled lysates were incubated with DAz-2:Cy5 click mix (25 μM as the final concentration; the composition of 1 mM DAz-2:Cy-5 click mix is as follows; 1 mM DAz-2, 1 mM cyanine 5(Cy5)-alkyne, 2 mM Cu (II)-TBTA complex, and 4 mM ascorbic acid in 15 mM PBS/30%(v/v) acetonitrile) at 37°C for 30 min, protected from light. The samples of cell lysates were reprecipitated by methanol/chloroform and the protein pellet was redissolved in 50 mM HEPES/2% SDS, and then added with equal volume of 2x Laemmli buffer (BioRad) supplemented with 10% β-mercaptoethanol. Samples were resolved by SDS-PAGE. Subsequently, gels were fixed in fixation buffer for 30 min, and then detected at 730 nm for the Cy5 signal that indicates protein persulfide levels and 488 nm for NBF–Cl signal (protein loading) on the Odyssey Fc imaging system (LI-COR, Lincoln, NE). Desired concentrations of ambroxol up to 100 μM were added in the cell culture medium for 48 h prior to preparing lysates, or applied directly to the cell lysates at 10 min prior to the start of gel electrophoresis.

2.14. Assays for CDDP-induced disturbance of DNA damages

The extents of DNA intercalation by CDDP that disturbs DNA supercoiling were quantified by pre-incubating 1 μg of plasmid (pcDNA3.1 empty vector, #V79020; Invitrogen) with serial concentrations of Na_2S_n (n = 1–4; 0.2, 0.5, 1.0, and 2.0 mM) in 10 mM phosphate buffer (pH 6.0) at room temperature for 5 min. Subsequently, CDDP was added to the solution to yield a final concentration 50 μM, followed by incubation of the reaction mixture at 37 °C for 60 min. After the reaction, the products were separated on 1% agarose gel to reproduce the DNA secondary structures. We also examined whether either GSH or hypotaurine at 1 mM ameliorates CDDP-induced disturbance of DNA supercoiling in vitro.

To determine DNA damages in CDDP-treated cells, we attempted to detect phosphorylation of histone H2AX (pH2AX) at sites of individual DNA double-strand breaks in cultured ovarian cancer cells. The pH2AX was examined by HCS DNA Damage kit (Thermo Fisher, H10292) according to previous methods [21,22].

3. Results

3.1. High-throughput proteomics reveals CSE as a prognostic marker

To identify protein biomarkers predictive of the efficacy of platinum-based chemotherapy in ovarian cancer after debulking surgery, an antibody library that consists of 1012 antibodies (Suppl. Tab. S1) was screened according to prognostic significance as recognized by automated quantitative virtual immunofluorescence pathology (AQVIP) with TMAs. AQVIP was developed as a novel high-throughput system to semi-quantify expression levels of antigens on TMAs using double-color immunofluorescent methods (Flow chart in Supplementary Fig. S1A) [23]. TMAs were stained with double-color immunofluorescence staining (Supplementary Fig. S1B) with the anti-cytokeratin 19 (CK19) antibody (green in Supplementary Fig. S1C) and with one of the antibodies listed in Suppl. Tab. S1. Briefly, an array template, onto which a white circle of spot templates was allocated at even intervals, was matched to the image of the TMAs. To detect the cancer area, which was stained with cytokeratin (CK)19 (Supplementary Fig. S1C, green) and to create a cancer mark, the target spot image was changed to binary image data using only the green color component (Supplementary Figs. S1D-E), distinguishing the white area as cancer. Expression levels of the individual antigens in cancer regions as marked by binary image data were quantified to determine the intensity of the red fluorescence (Supplementary Fig. S1F). The signal intensities per areas of cancer for each antigen in patients assigned from TMAs were automatically recorded in a storage computer (Supplementary Fig. 1A).

We prepared 2 independent cohorts of patients with ovarian carcinoma. Since the overall survival (OS) with each patient is involved in post-operative chemosensitivity, we firstly screened the proteins that predict OS using TMAs from a group of the patients (n = 135) who were treated in National Defense Medical College (NDMC), the first group is designated as the discovery cohort-NDMC. The second cohort was a group of patients in National Cancer Center (validation-NCC, n = 47), respectively, which aimed to examine whether candidate marker proteins screened by the training cohort-NDMC is predictive of prognosis

after the post-operative platinum-based chemotherapy (Table 1). We chose antibodies impacting OS ($p < 0.05$) for ovarian cancer as selected by the first and second screenings using the cohort-NDMC and the validation-cohort NCC. Cut-off values were calculated using X-tile algorithms [23].

The analyses in the discovery-NDMC cohort revealed that 3 antigens such as CSE, F-box-only protein 11 (FBXO11), and PCTAIRE protein kinase 1 (PCTK1) were identified as highly expressed markers associated with poor prognosis of ovarian cancer in which patients did not respond to the platinum-based chemotherapy. Fig. 1A depicted representative fluorescent immunohistochemistry showing the relationship between CK19 (in green) and CSE, FBXO11, or PCTK1 (in red). Kaplan-Meier analyses revealed significant differences in OS between patients with high (red lines) and low expressions (blue lines) of CSE ($p = 1.35 \times 10^{-7}$, log rank test), FBXO11 ($p = 0.0496$), and PCTK1 ($p = 0.0124$) in both the discovery cohort-NDMC and the validation-cohort NCC (log-rank test) (Fig. 1B). Cut-off points that were calculated to best distinguish prognoses of patients as shown by red triangles in x-axes of each histogram in Fig. 1B, when one of CSE, FBXO11 and PCTK1 was used under analyzing by X-tile algorithms to depict histograms of AQVIP scores. Red and blue bars in histograms of Fig. 1B showed the patients with high and low expressions of one of these proteins, respectively. As seen in the upper histogram, CSE expression varied among patients with poor prognosis. On the other hand, analyses of the discovery-NDMC cohort revealed that 9 antigens as low-expressed antigens associated with poor prognosis of ovarian cancer (Suppl. Figs. S3 Parts 1–3).

In the discovery-NDMC and validation-NCC cohorts, incidences of cases with high CSE expression were 13.3% (18/135) (Table 2) and 10.6% (5/47) (Table 3), respectively. When defining the risk of death by the value of hazard ratio (HR) of the patients' group with low CSE expression as 1.0, Cox univariate hazard analyses in the training cohort-NDMC showed that hazard ratios (HRs) for death with overexpression of CSE were 4.42 (95% confidence interval (CI), 2.44-8.01 $p = 9.06 \times 10^{-7}$). We thus further carried out multivariate analyses using the Cox proportional hazard model, and demonstrated that high expression of CSE (HR 2.86, 95% CI 1.18–6.90 $p = 0.020$) accounts for an independent

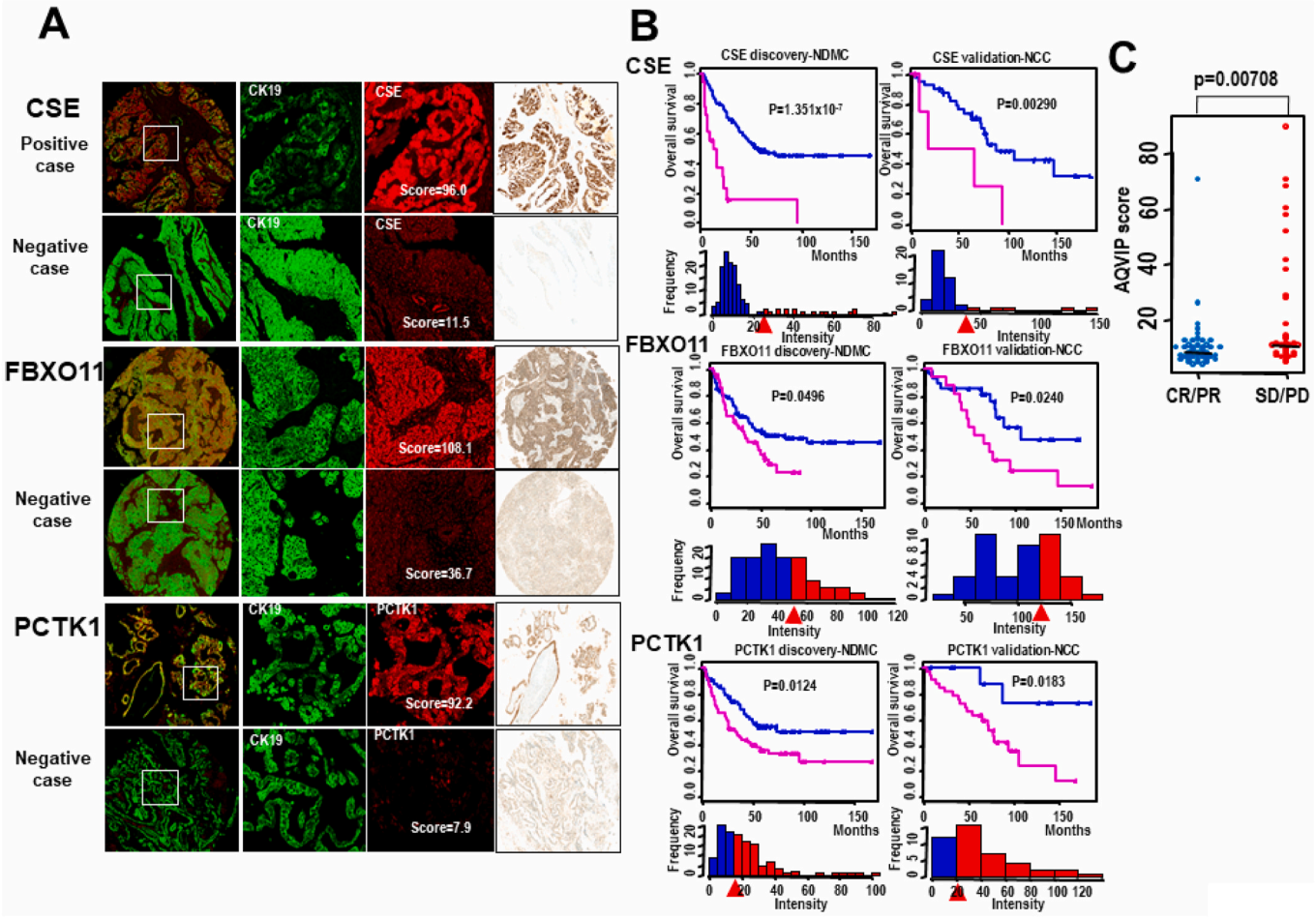

Fig. 1. Screening prognostic biomarkers for ovarian carcinoma patients undergoing postoperative platinum-based chemotherapy by high-throughput immunofluorescence pathology using tissue microarray (TMA).

Panel A. Immunofluorescence staining with anti-CK19 (green) antibody and, anti-CSE (red), anti-FBXO11 (red), or anti-PCTK1 antibody in tumors. Immunostaining with anti-CK19 antibody and anti-CSE, anti-FBXO11 (red), or anti-PCTK1 antibody (brown) in TMAs. In each immunofluorescence pictures, the upper and low panels show representative cases with high and low expressions, Scores represent intensities calculated by automated quantitative virtual immunofluorescence pathology (AQVIP) with TMAs. Panel B. Kaplan-Meier curves for overall survivals (OS) of CSE, FBXO11 and PCTK, and the intensitometries of individual protein expression in the discovery-NDMC and validation-NCC cohorts. Red and blue curves indicate prognosis of patients with high and low expressions of each protein, respectively. Histograms show intensities of the antibody-associated fluorescence in individual patients. Red triangles represent cut-off values for defining high and low groups. Differences were analyzed by log-rank test. Panel C. Differences in CDDP chemosensitivity between responder and non-responder patients in the training cohort-NDMC. Y-axis indicates CSE-associated AQVIP values. Blue and red dots show responder patients (CR: complete response, and PR: partial response) and non-responder patients (SD: stable disease, and PD: progressive disease), respectively, for the platinum-based chemotherapy. Differences between the responders and non-responders were analyzed by unpaired Student's t-test.

Table 2
Correlation of CSE expression with clinicopathological characteristics in the discovery cohort-NDMC[i].

	CSE expression		
	High RI[a] N = 18	Low RI[a] N = 117	*P* value[b]
Age			
56<	9	66	0.61
55≥	9	51	
FIGO stage[c]			
III	15	85	0.402
IV	3	32	
Histological type[d]			
Serous	1	86	<0.0001
Clear cell	14	11	
Endometrioid	1	9	
Mucinous	2	11	
Histological grade[e]			
1 or 2	3	37	0.1957
3	15	80	
Response to chemotherapy[f]			
Responders (CR/PR[g])	1	42	<0.0001
Non-responders (SD/PD[h])	10	22	

[a] Reactive intensity scores of automated quantitative virtual immunofluorescence pathology (AQVIP).
[b] Calculated by Chi-squared or Fisher exact test.
[c] According to the International Federation of Gynecology and Obstetrics (FIGO) staging system.
[d] According to the World Health Organization (WHO) criteria.
[e] According to Silverberg grading.
[f] According to the Response Evaluation Criteria for Solid Tumors (RECIST) guidelines (version 1.1).
[g] Complete response/partial response.
[h] Stable disease/progression disease.
[i] Four patients, whose tissue cores which were designed on tissue microarray were worn after deep sectioning, were excluded from the analysis.

Table 3
Clinicopathological association with CSE expression in the validation cohorts-NCC.

		CSE expression		
		High RI[a]	Low RI	
	N =	N = 5	N = 42	[d]p-value
Age	56<	3	19	0.654
	55≥	2	23	
Histological subtypes[b]	Clear cell carcinoma	4	4	0.002
	Others	1	38	
[c]Stage	III	3	34	0.28
	IV	2	8	

[a] Reactive intensity scores of automated quantitative virtual immunofluorescence pathology (AQVIP).
[b] According to the International Federation of Gynecology and Obsterics (FIGO) staging system.
[c] According to the World Health Organization (WHO) criteria.
[d] Fisher's exact test.

prognostic factor for death of ovarian cancer in patients who underwent platinum-based chemotherapy after debulking surgery (Table 4). On the other hand, histological type, but not histological grade, showed statistical significance in the Cox univariate hazard analyses, but no significance in the multivariate hazard analyses (Table 4). The results of Cox uni- and multi-variate analyses for other 11 candidates revealed that the protein expression of CSE and PCTK1 only remained as independent factors in the discovery cohort-NDMC (Suppl. Fig. S4, Parts 1–2). These results collectively suggest that high CSE expression in ovarian carcinoma is an independent determinant to predict the prognosis for overall survival of the patients with ovarian cancer who underwent the post-operative platinum-based chemotherapy after debulking surgery.

Using the discovery cohort-NDMC (Table 2), we compered the AQVIP scores of individual patients (n = 75) who were able to be evaluated by Response Evaluation Criteria in Solid Tumors (RECIST) guideline with chemosensitivity. We defined the responders (n = 43) as the complete response (CR) and partial response (PR), the non-responders (n = 32) as the stable disease (SD) and partial response (PR). The efficiency of chemotherapy was evaluated according to RECIST guideline. The AQVIP scores for CSE of non-responders (SD/PD) were significantly higher than those of the responders (CR/PR) (Fig. 1C). Among proteins analyzed, these results collectively showed that CSE is the best predictor of the efficacy for the platinum-based chemotherapy. Analyses of other marker candidates (Fig. 1) revealed that only CSE predicts both the efficacy for platinum-based chemotherapy and prognosis based on survival times.

3.2. The SERS signal at 480 cm^{-1} predicts overall survival of CCC patients after surgery

As seen in the correlation of CSE expression with clinicopathological findings in the discovery-NDMC cohort (Table 2), 98.9% (86/87) of serous adenocarcinoma (SAC) exhibited low reactive intensity scores (RI). The percentages of high RI scores were also small in endometrioid and mucinous carcinomas. On the other hand, as many as 56% (14/25) of clear cell carcinoma (CCC) displayed the high RI scores. Such a difference between SAC and CCC was reproduced in the NCC-cohort (Table 3), suggesting that CCC constituted a major histological type with significantly greater CSE expression than other histological types, while the magnitude of CSE expression varied robustly among individual CCC cases.

These data led us to further examine roles of CSE-derived metabolites for CCC chemoresistance using large-area surface-enhanced Raman spectroscopy (L-SERS): The system allowed us to detect pixel-based Raman scattering light generated from sulfur-containing metabolites such as glutathione, hypotaurine, and polysulfides which occurred in tissue slices attached to the surface of GNF-SERS substrate (Suppl. Fig. S2) [4]. To determine specific SERS spectral wave numbers of cancer regions of CCC and SAC, we averaged spectra of 15 CCC and 12 SAC cases who did not receive neo-adjuvant chemotherapy prior to the surgery (Suppl. Fig. S5A) by calculating the peak signal intensities of these peaks with ±10-cm^{-1} widths. Our previous studies suggested that the SERS peaks at 298 cm^{-1}, 480 cm^{-1} and 978 cm^{-1} indicate the presence of reduced glutathione (GSH), polysulfides, and hypotaurine [4], respectively, which yields signals through interactions between gold atoms on nanoparticles of the GNF substrate and S-containing metabolites. Among them, the spectra showed the peaks at 296 cm^{-1}, 480 cm^{-1} and 720 cm^{-1} in CCC (Suppl. Fig. S5A). The peak at around 720 cm^{-1} was likely to give rise to a vibrational mode which is mainly yielded by purine metabolites [4,15], and was comparable between CCC and SAC. On the other hand, we examined one frozen section of fresh noncancerous ovarian tissues stored in NCC Biobank which was obtained from a patient with colon cancer coinciding with uterine leiomyoma who underwent hysterectomy and adnexectomy (Suppl. Figs. S5B-C), showing that the peak at 480 cm^{-1} does not occur in the non-cancerous ovarian tissue.

The SERS signals at 480 cm^{-1} were visualized as two-dimensional micrographs. Pathological annotation showing cancer regions (yellow in Fig. 2A) and stroma (green in Fig. 2A) revealed that CCC exhibited robust SERS signal at 480 cm^{-1} in cancer cell nests and stromal regions (Fig. 2B). Immunoreactivities of CSE were mainly localized in cancer cell nests rather than in stromal regions (Fig. 2C). On the other hand, SAC displayed weaker SERS signal at 480 cm^{-1} with only few CSE immunoreactivities (Fig. 2D–F). The SERS signal intensities in both cancer cell nests and stromal regions at 480 cm^{-1} varied largely among individual CCC patients (Fig. 2G and H). As judged by empirical cumulative provability analyses, the CSE immunoreactivities and the SERS signal

Table 4
Hazard ratios for death in advance ovarian cancer patients of the training cohort-NDMC[f].

			Univariate analysis			Multivariate analysis		
	Number of cases		HR[a]	95% CI[a]	*P* value[b]	HR[a]	95% CI[a]	*P* value[e]
CSE RI score[a]								
	High	18	4.42	2.44–8.01	9.06×10^{-7}	2.86	1.18–6.90	0.020
	Low	117						
Age								
	56<	75	1.47	0.91–2.40	0.12			
	55≥	60						
FIGO stage[b]								
	III	100	2.00	1.23–3.25	0.0048	1.76	1.07–2.90	0.026
	IV	35						
Histological type[c]								
	Other	110	2.83	1.67–4.83	0.0001	2.09	0.92–4.74	0.078
	Clear cell carcinoma	25						
Histological grade[d]								
	1 or 2	40	1.54	0.89–2.66	0.119			
	3	95						
Residual tumor after surgery								
	0–2 cm	60	2	1.23–3.25	0.0053	2.11	1.25–3.56	0.0052
	>2 cm	75						

Four patients, whose tissue cores were worn after deep sectioning, were excluded from the analysis.
[a] Abbreviations: HR, hazard ratio; CI, confidential interval; RI score, Reaction Intensity score.
[b] According to the International Federation of Gynecology and Obsterics (FIGO) staging system.
[c] According to the World Health Organization (WHO) criteria.
[d] According to Silberberg grading.
[e] Cox proportional hazards regression model.
[f] Four patients, whose tissue cores which were designed on tissue microarray were worn after deep sectioning, were excluded from the analysis.

intensities in cancer cell nests varied significantly among CCC patients (Fig. 2I and J). We defined the two subgroups with high and low SERS intensities at 480 cm^{-1} using the median as a cut-off value (Fig. 2K). As seen, CCC patients with greater SERS signals at 480 cm^{-1} displayed significantly shorter survival times than those with lower SERS signals after the surgery, suggesting that the higher signal at 480 cm^{-1} serves as a predictive marker of the overall survival of CCC patients.

As we reported previously [4], the GNF-SERS signals at around 450–480 cm^{-1} suggest the presence of sulfane-sulfur bonds of polysulfides, as indicated by SERS spectra of inorganic polysulfides (Suppl. Fig. S5D); this issue will be discussed later in Fig. 3. We compared 2 different SERS signals for GSH and hypotaurine: The peaks at 298 cm^{-1} (GSH) and those at 978 cm^{-1} (hypotaurine) did not differ between CCC and SAC in both cancer cell nests and stromal regions (Suppl. Fig. S5E).

3.3. *Characterization and comparison of polysulfide signals in vivo and in vitro*

Polysulfides are known to be degraded by monobromobimane (mBBr), a derivatizing electrophilic reagent that cleaves sulfane sulfur bonds to generate SDB (see the formula of Fig. 3A). To note is the fact that the standard compound of mBBr did not generate any evident SERS peaks, but SDB generated the SERS peaks at 452 cm^{-1} and 583 cm^{-1} (Fig. 3A). On the other hand, the peak yielded by Na_2S_3 at 460 cm^{-1} was vanished by applying mBBr, and generated the *de-novo* main peak at 590 cm^{-1} with smaller peaks at 441 cm^{-1} and 534 cm^{-1}, suggesting that new products generated after the mBBr application involve SDB (Fig. 3B).

As shown in Fig. 2B and Suppl. Fig. S5D, there is a gap of wave numbers between the SERS signal in ovarian cancer tissues (480 cm^{-1}) and that observed in inorganic polysulfides (420-460 cm^{-1}). We thus examined SERS spectra of organic polysulfides which were known to occur in vivo [4,16]. Oxidized glutathione trisulfide at 200 μM exhibited a peak at 305 cm^{-1} which suggested the Au–S vibrational mode on SERS substrates [4], but the asymmetric peak indicating the sulfane-sulfur bond was not detected around at 460–480 cm^{-1} (Fig. 3C). On the other hand, the same concentration of cystine trisulfide at 200 μM displayed a robust peak at around 300 cm^{-1} (Au–S vibration) and the peak at 477 cm^{-1} (Fig. 3D): Furthermore, application of monobromobimane (mBBr) to cystine trisulfide diminished the peaks at 477 cm^{-1}, and generated the three peaks at 451 cm^{-1}, 533 cm^{-1} and 588 cm^{-1}, suggesting the formation of SDB through reacting cystine trisulfide with mBBr (Fig. 3E). These results suggest that the SERS peak at 480 cm^{-1} in vivo accounts for organic polysulfides including cystine trisulfide to share the sensitivity to mBBr.

Considering these data in vitro, we topically applied a 1-μl drop of the mBBr solution at 5 mM on the surface of tissues, and collected SERS signal through the inverted microscope, and finally performed HE staining in situ (Fig. 3F); In good agreement with the results in Fig. 3A and B, the on-tissue mBBr application diminished the SERS signal at 480 cm^{-1} (Fig. 3G). Simultaneously, a topical on-tissue mBBr application generated the SDB-associated SERS images at 452 cm^{-1} and 583 cm^{-1} (Fig. 3H and I). The newly generated images at 452 cm^{-1} and 583 cm^{-1} were demarcated to the polysulfide-associated SERS image at 480 cm^{-1}. Furthermore, the ratio of SERS signal intensities between 583 cm^{-1} and 480 cm^{-1} in the mBBr-applied cancer regions was significantly greater than the mBBr-free cancer regions (Fig. 3J), suggesting that SDB generation by on-tissue mBBr application serves as evidence for the presence of endogenous polysulfides, being consistent with previous studies in vitro [4,16,24,25].

Data shown in Fig. 2 indicated that polysulfide-associated SERS signals in CCC were greater than those in SAC, but with greater variance among individual cases. To minimize individual variances among different specimens [4,12], the presence of organic hydropersulfides such as GSSH or Cys-SSH was indirectly examined by composing the ratio images of glutathione S-sulfonate ($GSSO_3^-$) versus glutathione sulfonate (GSO_3^-) and cysteine S-sulfonate ($Cys\text{-}SSO_3^-$) versus cysteine sulfonate ($Cys\text{-}SO_3^-$); these sulfonated compounds are yielded by irreversible oxidation of glutathione hydropersulfide (GSSH) and cysteine hydropersulfide (Cys-SSH), respectively [8,13]. The ratios of $GSSO_3^-/GSO_3^-$ and $Cys\text{-}SSO_3^-/Cys\text{-}SO_3^-$ were significantly elevated in cancer cell nests of CCC than in those of SAC (Fig. 4A and B). To be noted is that cancer cell nests (asterisks in Fig. 4A) exhibited robust intensities of the ratio, suggesting that hydropersulfide generation is upregulated in these regions. Overproduction of these compounds was also seen in stromal regions of CCC tissues, besides the difference in the

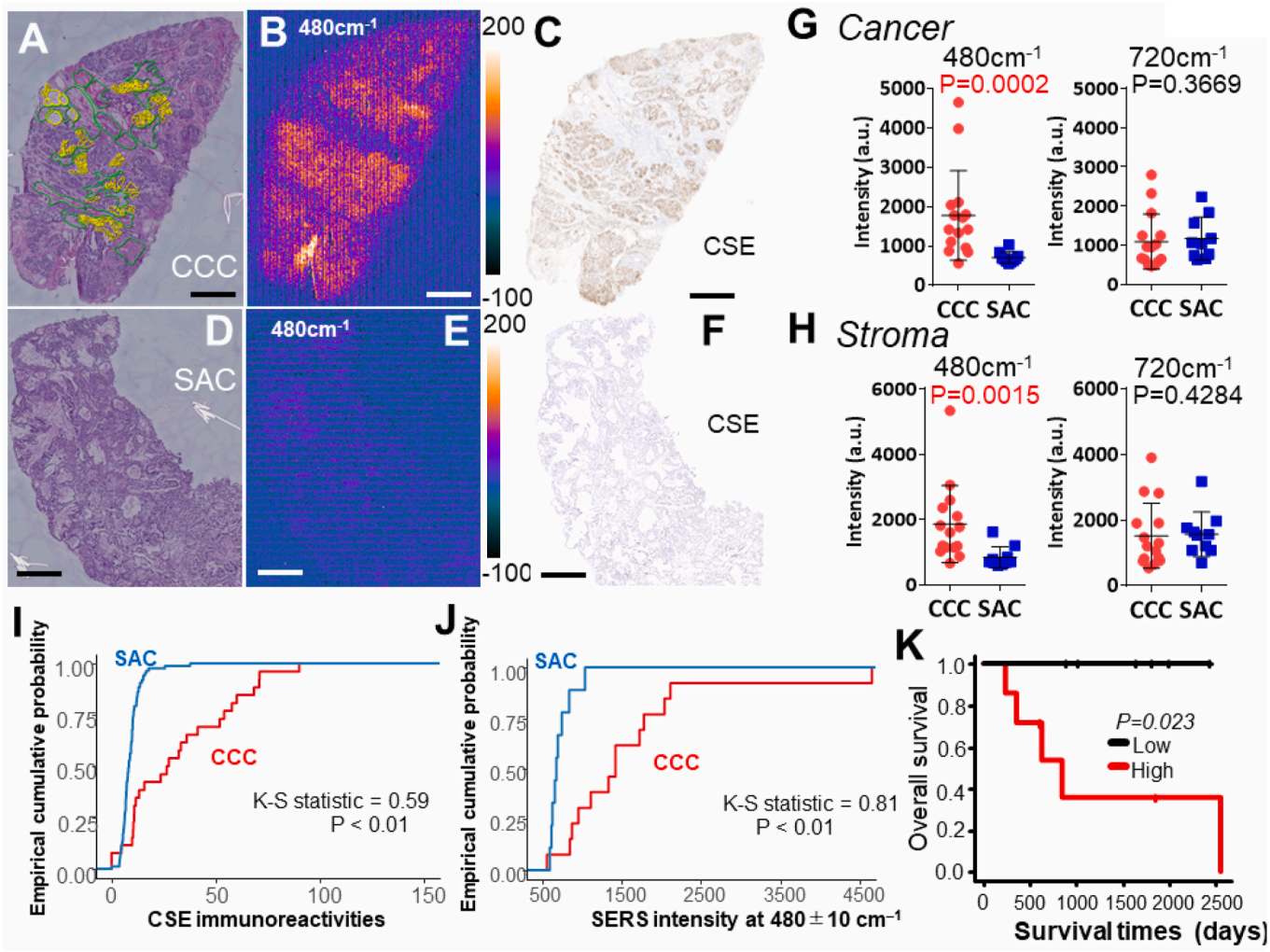

Fig. 2. On-tissue visualization of polysulfides by SERS imaging in tissue sections derived from clear cell carcinoma (CCC) and serous adenocarcinoma (SAC). Panels A and B. Representative pictures of H-E staining and SERS imaging at 480 cm^{-1} in CCC tissue slices, respectively. H-E staining was performed after acquiring the SERS image in the same tissue slice. Yellow and green regions in Panel A indicate annotated regions of cancer cell clusters, and cancer stroma, respectively. Panel C. A representative picture of immunohistochemistry for CSE in the serial section of CCC. Panels D and E. Representative pictures of H-E staining and SERS imaging at 480 cm^{-1} in SAC tissue slices, respectively. H-E staining was performed after acquiring the SERS image in the same tissue slice. Panel F. A representative picture of immunohistochemistry for CSE in the serial section of SAC. All bars indicate 1 mm. Panels G and H. Differences in SERS signals in cancer cell nests and stromal regions at 480 cm^{-1} and 720 cm^{-1} between CCC (n = 15) and SAC (n = 10) tissue slices. Intensities are expressed as arbitrary units (a.u.) and mean ± SE. SERS signals were accumulated within ±10 cm^{-1} at each wave number. Panels I and J. Differences empirical cumulative probability of CSE immunoreactivities and SERS signal intensities at 480 cm^{-1} in the cancer cell nestsbetween CCC and SAC tissue slices. K–S denotes Kormogolov-Smirnov analyses. SERS signals were accumulated within ±10 cm^{-1} at each wave number. Panel K. Differences in Kaplan-Meier curves for overall survivals (OS) between CCC patients with greater polysulfide signals (Red line, n = 7) and those with smaller signals (Blue line, n = 6). Groups were divided by median of the SERS intensities among 13 patients. Among 15 CCC patients, prognosis of 2 CCC patients were unable to trace OS after the surgery. The p value was 0.023 in log-rank test.

$GSSO_3^-/GSO_3^-$ ratio in the stroma was only marginally significant. Considering that different RSS constitute a network to exchange reducing and oxidizing equivalents, these results were consistent with a notion that CCC generates hydropersulfides robustly in cancer cell nests.

3.4. Ambroxol degrades polysulfide to unlock chemoresistance in cancer cell lines

As shown in Supplementary Tab. 1, expression of CBS, another RSS-generating enzyme, did not differ between responders and non-responders with ovarian carcinomas. Immunohistochemistry of mercaptopyruvate sulfotransferase (MPST), an RSS-generating mitochondrial enzyme, did not differ between CCC and SAC cases (Fig. 5A). Further studies using 9 different ovarian cancer cell lines showed that CBS, MPST and CARS2 were comparably expressed, except RMUG-S in which CBS was undetectable. Among them, OVISE and OVTOKO represented characteristics of CCC, in that they expressed robust CSE expression versus other cell lines (Fig. 5B and C). CARS2 knockdown did not suppressed SDB contents of OVISE cells (Fig. 5D and E). We thus compared amounts of SDB, a terminal product derived from polysulfides in the presence of mBBr, in two different cell lines expressing CSE, that is, OVISE and OVTOKO versus OVCAR-3 which expressed little CSE expression. Notably, SDB amounts in OVISE and OVTOKO were significantly greater than those of OVCAR3 (Fig. 5F).

We further inquired whether CSE knockdown in OVISE cells altered RSS generation. Treatment of the cells with shCSE suppressed expression of CSE but not that of CBS, MPST and CARS2 (Supplementary Fig. S6A). The shCSE treatment suppressed CD44v expression but not CD44s expression of the cells (Supplementary Fig. S6B). Under these circumstances, amounts of SDB was significantly suppressed by shCSE (Supplementary Fig. S6C), showing significant but partial inhibition of polysulfides. On the other hand, GSH, hypotaurine and taurine became

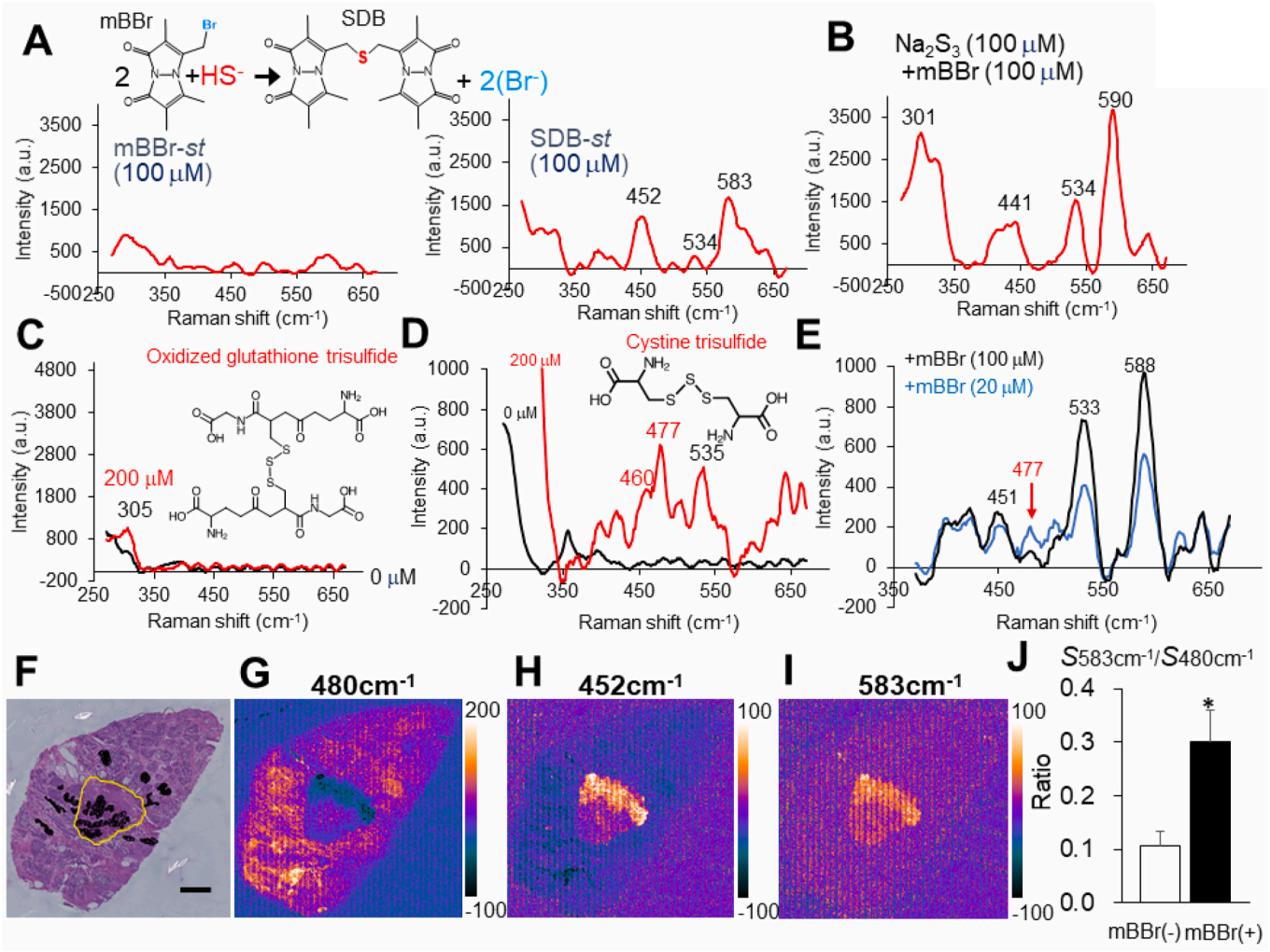

Fig. 3. Characterization of SERS spectra of inorganic and organic polysulfides in vitro and the mBBr-elicited changes to generate SDB in vivo. Panel A. Characterization of SERS spectra for mBBr and SDB. The left and middle panels indicate representative SERS spectra for the standard mBBr (mBBr-*st*) and SDB (SDB-*st*) at 100 μM. The upper formula shows the reaction showing derivatization of SH^- by mBBr to generate SDB. Panel B. A representative SERS spectrum of Na_2S_3 at 100 μM and the alterations by adding mBBr at 100 μM. Panels C–D. Representative SERS spectra of oxidized glutathione trisulfide and cysthine trisulfide, respectively. Panel E. Mixture of cystine trisulfide at 200 μM with monobromobimane (mBBr) abolishes the SERS peak at 480 cm^{-1} and generates new peaks at 451 cm^{-1}, 533 cm^{-1} and 588 cm^{-1}, indicating synthesis of SDB. Panel F. A representative picture of H-E staining with annotation of cancer cells which was shown as black regions. H-E staining and pathological annotation were performed in the identical tissue section after the SERS data shown in Panels G–I were collected. A tellow circle indicates the region of the topical mBBr application. Panel G. A representative SERS image at 480 cm^{-1} after the topical mBBr application. Panels H and I. Representative SERS images at 452 cm^{-1} and 583 cm^{-1}, respectively, in the identical tissue section of CCC in Panel b. SERS signals were accumulated within ±10 cm^{-1} at each wave number. The tissue slice of CCC in Fig. 3 is a semi-serial section of that shown in Fig. 2. Color bas indicates the SERS signal intensity (a.u.). Panel J. The SERS signal ratio between the signal at 583 cm^{-1} ($S583cm^{-1}$) and that at 480 cm^{-1} ($S480cm^{-1}$) in the mBBr-free regions (mBBr(−)) and mBBr-applied regions (mBBr(+)). Data indicate mean + SEM of 3 separate samples from different individuals. *p = 0.044 analyzed by paired Student's t-test. (For interpretation of the references to color in this figure legend, the reader is referred to the Web version of this article.)

significantly higher in the CSE-knockdown cells, presumably because of compensation of these metabolites through residual CD44s/xCT mechanisms (Supp. Fig. S6D).

These lines of data led us hypothesize that, not CSE targeting, but application of compounds that directly degrade endogenous hydropersulfides or polysulfides may serve as an adjuvant strategy that enhances CDDP-induced death of ovarian cancer cells such as OVISE or OVTOKO. Ambroxol has been known to be utilized for adjuvant therapy for lung cancer [26,27]. Our serendipitous observation revealed that ambroxol, an expectorant drug that cleaves disulfide bonds of mucin, has the potent ability to degrade sulfane-sulfur bonds of Na_2S_4 in a dose-dependent manner (Fig. 6A and B). We found that ambroxol at 25 μM for 72 h did not trigger any significant annexin V translocation as an index of cell death against OVISE and OVCAR3 cells in culture. However, with greater concentrations of ambroxol, OVISE cells exhibited significant increases in cell death versus OVCAR3 cells (Fig. 6C). Using 25 μM ambroxol, we examined its tumoricidal effects on CDDP-resistant OVISE cells. As seen in Fig. 6D, CDDP treatment for 48 h caused only modest increases in the annexin V translocation (open bars in Fig. 6D): Under these circumstances, co-incubation with ambroxol significantly enhanced the dose-dependent annexin V translocation to result in significant augmentation of the cell death (closed bars in Fig. 6D). On the other hand, SAC-representing OVCAR3 cells exhibited dose-dependent increases in the CDDP-induced annexin V translocation, while displaying no further enhancement of the cell death by adding the same concentration of ambroxol (Fig. 6E). We also examined effects of ambroxol on the polysulfide-overproducing OVTOKO cells, showing further enhancement of the CDDP-induced cell death, and repressed by applying GYY4137, a slow-releasing donor of hydrosulfide anion (Fig. 6F) [28].

Under the same culture conditions with the earlier time at 24 h, we

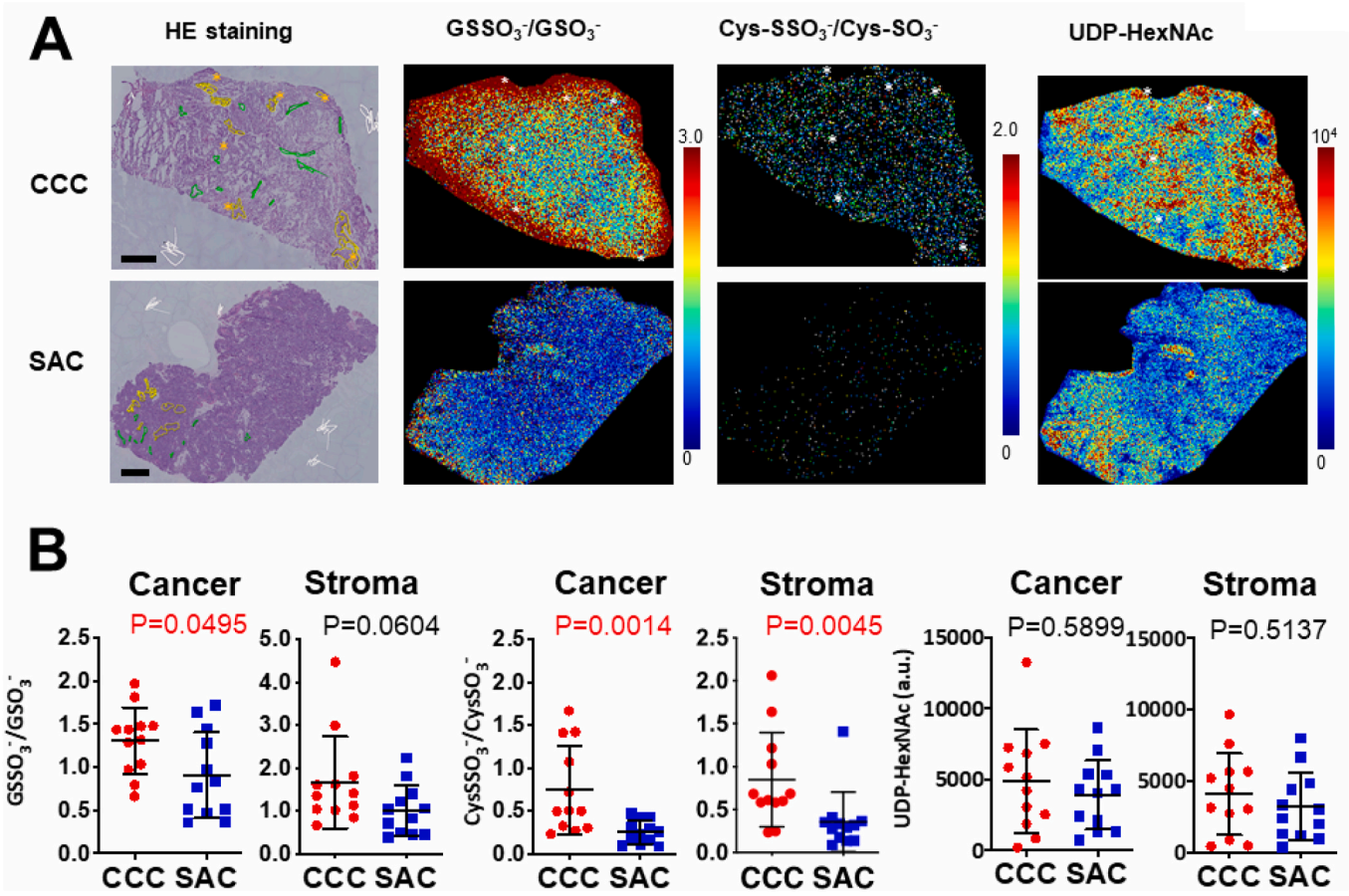

Fig. 4. Imaging detection of glutathione persulfide and cysteine persulfide in CCC.
Data indicates representative pictures of glutathione S-sulfonate ($GSSO_3^-$) and cysteine S-sulfonate ($Cys\text{-}SSO_3^-$), irreversibly oxidized products of reduced glutathione persulfide and cysteine hydropersulfide under atmospheric pressure MALDI conditions, respectively. Panel A. The mass signals of $GSSO_3^-$ and $Cys\text{-}SSO_3^-$ were standardized by composing the ratio images of $GSSO_3^-$ versus glutathione sulfate ($GSSO_3^-/GSO_3^-$), and $Cys\text{-}SSO_3^-$ versus cysteic acid ($Cys\text{-}SSO_3^-/Cys\text{-}SO_3^-$), respectively, which serve as markers of hydropersulfide species according to our previous method [4,11]. UDP-HexNAc; UDP-N-acetylhexosamine. Regions with asterisks indicate localization of cancer cell nests which was surrounded by yellow annotations. Annotations in green indicate cancer stromal regions. Panel B indicate comparison of the signal ratios of $CysSSO_3^-$/Pi between CCC and SAC. Note that the ratios of $GSSO_3^-/GSO_3^-$ are significantly greater in CCC than those in SAC. The ratio of $Cys\text{-}SSO_3^-$ versus $Cys\text{-}SO_3^-$ appeared higher in CCC, but only with marginally significant difference. $P < 0.05$ analyzed by Mann-Whitney's *U* test. The number of CCC and SAC patients from which samples were collected was 12 for each group. Data were expressed as mean ± SE values.

attempted to detect the initial DNA damages in cells by determining phosphorylation of histone H2AX (pH2AX) at sites of individual DNA double-strand breaks in cells. As seen, both OVISE and OVCAR3 cells exhibited dose-dependent increases in the pH2AX expression versus cell numbers (Hoechst). However, addition of ambroxol at 25 μM caused a significant increase in the pH2AX in OVISE cells (Fig. 6G) but not in OVCAR3 cells (Fig. 6H). These results reveal crucial roles of ambroxol as the polysulfide-degrading compound for unlocking chemoresistance of OVISE cells against CDDP. Furthermore, data in the xenograft transplantation model using OVISE cells in vivo in nude mice showed that co-administration of ambroxol with CDDP significantly enhanced CDDP-induced regression of tumour volumes (yellow and blue lines in Fig. 6I).

3.5. Ambroxol diminishes CSE-dependent protein persulfidation in cancer cells

High concentrations of mBBr treatment degrade hydropolysulfides to yield SDB as a final stable product. If ambroxol degrades organic and inorganic hydropolysulfides in cells, SDB contents may be increased after the ambroxol treatment. Treatment of protein-free cell lysates of OVISE and OVTOKO cells caused significant increases in SDB contents (Fig. 7A). These results led us to inquire whether protein persulfides, if any, can be degraded by the ambroxol treatment in cells or in cell lysates. Fig. 7B indicated that OVTOKO cells showed the highest DAz2-Cy5 fluorescence as an indicator of protein persulfides (PSSH) that were visualized by dimedone switching assay [19,20]. The fluorescence was abolished with sgCSE treatment to knockout CSE, suggesting that CSE plays a critical role for PSSH generation. We next compared differences in PSSH levels among OVISE, OVTOKO and OVCAR3 cells: OVTOKO showed the greatest, OVISE showed modest, and OVCAR3 indicated the lowest PSSH signals (Fig. 7C). These results were in good agreement with results of SDB measurements in Fig. 5F. PSSH signals in OVISE cells were remarkably suppressed by co-incubation with ambroxol for 48 h in culture (Fig. 7D). Furthermore, direct application of 100 mM ambroxol to protein-containing cell lysates caused visible decreases in PSSH signals in OVISE and OVTOKO cells. These results suggest that ambroxol enables to degrade protein persulfides and to increase SDB products.

3.6. Polysulfide protects against CDDP-induced damages of DNA structure

High CSE expression with greater signal of polysulfides in CCC led us to further investigate whether polysulfides might directly react with CDDP and thereby interfere with DNA damages in cancer cells. Since CDDP enables intercalation between bases of the double-strand structures of DNA and thereby causes structural changes and disturbance of

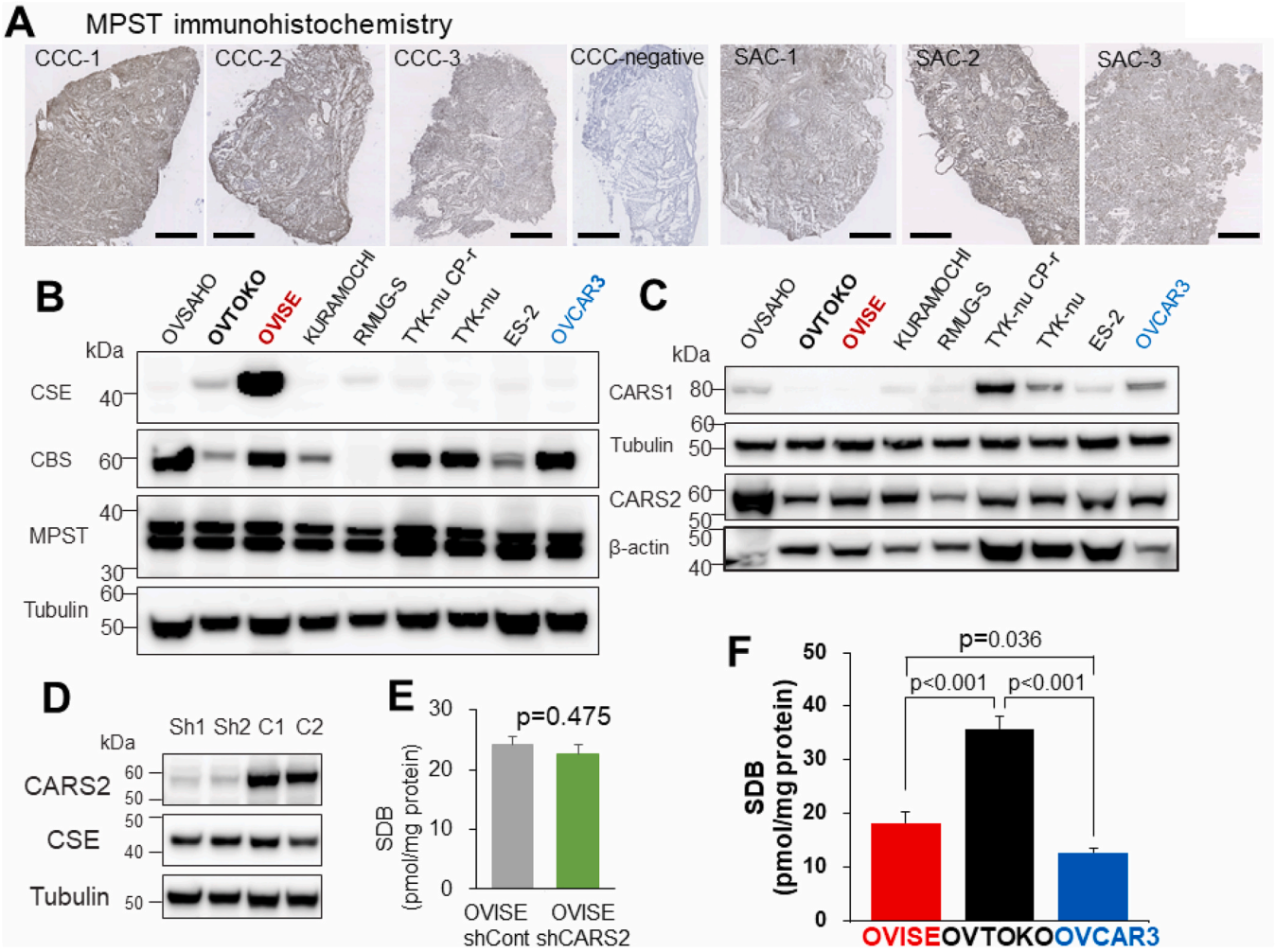

Fig. 5. Immunohistochemistry of 3-mercaptopyruvate sulfotransferase in ovarian cancer and RSS-generating enzymes expressed in different cancer cell lines.
Panel A: Expression of 3-mercaptopyruvate sulfotransferase (MPST) was analyzed in 3 separate patients with clear cell carcinoma (CCC) or with serous adenocarcinoma (SAC). Three representative cases of CCC and SAC are shown. Bars represent 1 mm. Negative control: Non-specific IgG staining by using the tissue slice collected from a patient with CCC. Panel B: Differences in the expression of CSE, CBS, and MPST among cell lines. Note that OVISE shows robust CSE expression. The expression of MPST is comparable among ovarian cancer cell lines. Panel C: The expression of CARS1 and CARS 2 in these cell lines. Note that OVCAR3, but not OVISE, expresses CARS1. The expression of CARS2 is comparable among the cell lines examined. Panel D: The establishment of OVISE cell lines with CARS2 knockdown. Note no remarkable changes in CSE expression by treatment with 2 different constructs of shCSE. Panel E: Effects of CARS2 knockdown on sulfodibimane (SDB) contents. Panel F: Differences in the amounts of sulfodibimane (SDB), a metabolite derived from the chemical reaction of polysulfides with monobromobimane in vitro. One-way ANOVA with Fischer's LSD test. $F(2, 39) = 26.790$.

DNA supercoiling [29,30], we determined CDDP-induced alterations in bulk molecular volumes of supercoiled DNA and their recovery by the application of polysulfides in vitro. CDDP induced an increase in the bulk molecular volume of double-stranded DNA, suggesting the interference with its supercoiling state (Fig. 8A). The addition of increasing concentrations of donors of hydrogen sulfide (Na_2S) and different hydropolysulfides (Na_2S_x: x = 2–4) dose-dependently repressed the CDDP-induced increase in the molecular volume of double-stranded DNA. Notably, the repressing effects of hydrogen polysulfides became greater with the increasing number of sulfur atoms in each polysulfide (Fig. 8A). Conversely, GSH and hypotaurine at physiological concentrations (mM) showed no repressing effects on CDDP-induced disturbance of DNA supercoiling (Fig. 8B and C). To determine whether CDDP directly interacts with hydropolysulfides such as Na_2S_4, we performed non-SERS conventional Raman scattering (Fig. 8D and E). The non-SERS Raman spectrum of CDDP was characterised by 4 major peaks at 316 cm^{-1}, 327 cm^{-1} (Cl–Pt–N), 504 cm^{-1}, and 522 cm^{-1} (Pt–N) (Fig. 8D). These results are in good agreement with those of a previous study [29]. The addition of Na_2S_4, a hydrotetrasulfide donor, caused the disappearance of these CDDP peaks (Ci-Pt-N and Pt–N), and the CDDP vanished the peak yielded by Na_2S_4 in a dose-dependent manner (Fig. 8E). These results suggested that CDDP reacts with polysulfides and loses its DNA-intercalating ability in vitro. Such an action of polysulfides in vitro was not shared by GSH or hypotaurine at physiological concentrations.

4. Discussion

The high-throughput automated system to compare semi-quantitatively the many proteins expressed on the tissue slices of solid cancer [31] enabled us to determine CSE as a marker protein that determines resistance to platinum-based chemotherapy and poor prognosis after debulking surgery. CSE catalyzes the α− and γ-elimination of cystathionine to form cysteine, α-ketobutylate, and NH_3, and serves as one of the three principal enzymes involved in the endogenous production of H_2S, and the other H_2S-generating enzymes are CBS and 3-MST [2,5,32,33]. Thiols, H_2S, and RSS including polysulfides, constitute a sulfur-sinking metabolic network in which reducing

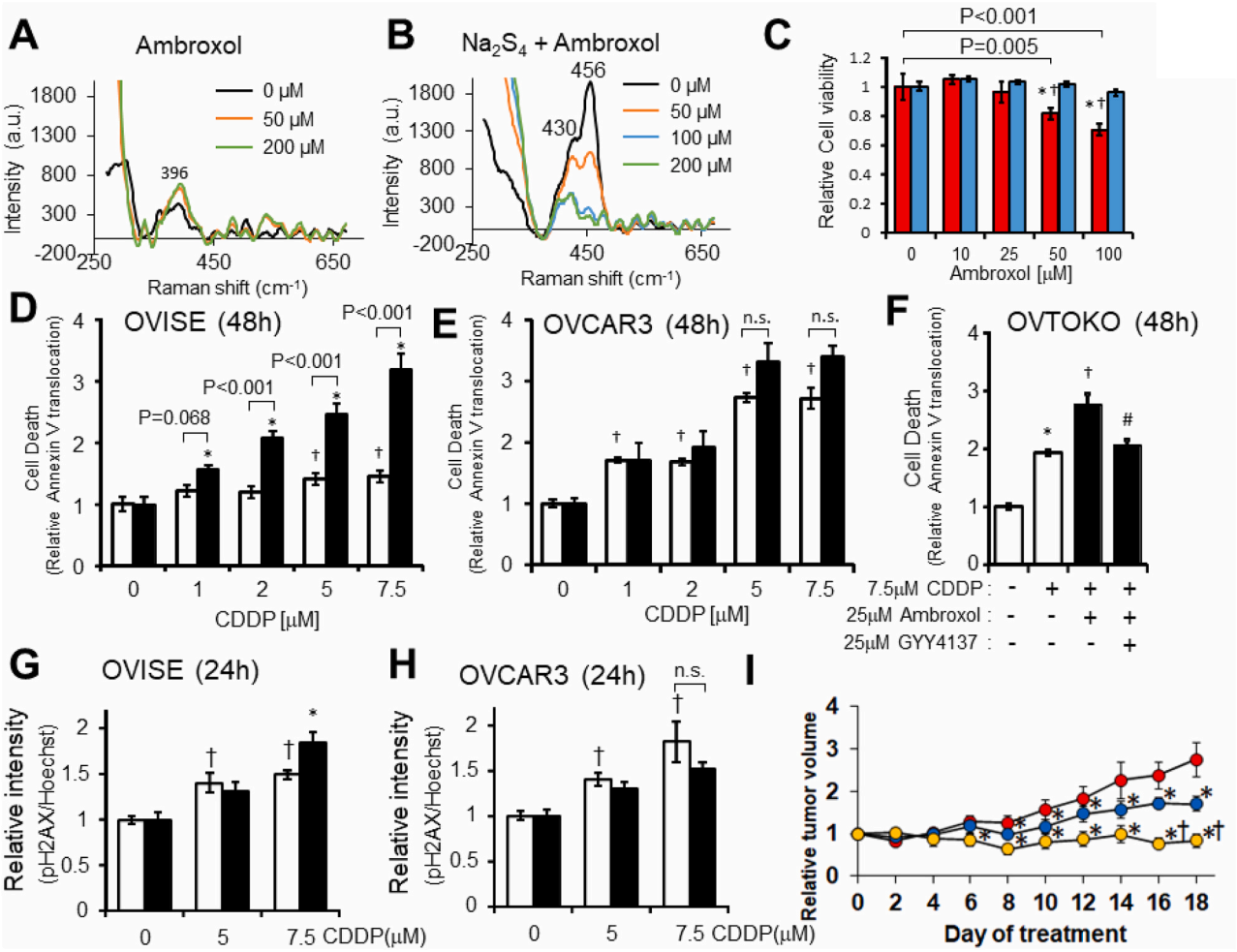

Fig. 6. Effects of ambroxol, a polysulfide-degrading compound, on CDDP-induced cell death. Panels A and B: SERS spectra of ambroxol in the absence or presence of Na_2S_4. The concentration of Na_2S_4 was 100 μM. Panels C: Panel C: Effects of increasing concentrations of ambroxol on the viability of OVISE (red) and OVCAR-3 (blue) cells. P values less than 0.05 were considered statistically significant according to one-way ANOVA with Fischer's LSD test throughout Fig. 6 (n = 4). F(9, 39) = 20.005. Panels D and E: Effects of ambroxol at 25 μM on CDDP-induced death of OVISE and OVCAR3 cells. Cell death was assessed using the annexin V translocation assay. *$P < 0.05$ as compared with ambroxol-free group (open bars) treated with CDDP alone.†$P < 0.05$ as compared with CDDP-free controls. F(9,39) = 30.171 and F(9, 39) = 22.989 in Panel D and E, respectively. Panel F: Effects of CDDP in OVTOKO cells. Likewise that in OVISE cells, the cell death was significantly enhanced by adding ambroxol at 25 μM, and repressed significantly by adding GYY4137, a slow-releasing hydrosulfide donor. *P < 0.05 as compared with ambroxol- and CDDP-free group (n = 4). †P < 0.05 as compared with the CDDP-treated group in the absence of ambroxol. #P < 0.05 as compared with the group treated with CDDP and ambroxol in the absence of GYY4137. F(3,15) = 44.430. Panels G and H: Alterations in phosphorylation of histone H2AX (pH2AX) at sites of individual DNA double-strand breaks in OVISE and OVCAR3 cells, respectively. The culture conditions are identical with those in Panels D and F, besides time to collect samples was 24 h after CDDP treatment in the absence (open bars) or presence (closed bars) of 25 μM ambroxol. OVISE and OVCAR3 cells exhibited dose-dependent increases in the relative intensities of pH2AX expression versus cell numbers (Hoechst). However, addition of ambroxol at 25 μM caused a significant increase in the pH2AX in OVISE cells (Panel A) but not in OVCAR3 cells (Panel B). *$P < 0.05$ as compared with ambroxol-free group (open bars) treated with CDDP alone. †$P < 0.05$ as compared with CDDP-free controls. F(5, 35) = 11.180 and F(5, 35) = 7.584 for Panels G and H, respectively. Panel I: Effects of co-administration of ambroxol on CDDP-induced regression of tumour volumes of OVISE xenografts in nude mice. Red, blue and yellow circles and bars indicate groups treated with OVISE transplantation alone (N = 8), with OVISE + CDDP (n = 10), and with OVISE + CDDP + ambroxol (n = 7), respectively. mean ± SEM of separate data were analyzed. Tumour volumes were standardized by the data at day 0 which is 10 days after the OVISE transplantation. *P < 0.05 versus OVISE transplantation alone. †P < 0.05 versus OVISE + CDDP. F(2, 22) at 18 days = 16.291. Data were analyzed by one-way ANOVA with Fischer's LSD test. (For interpretation of the references to color in this figure legend, the reader is referred to the Web version of this article.)

equivalents are interchangeable among different RSS. Among these species, inorganic polysulfides are unstable and tend to decompose to H_2S and elemental sulfur and possess the ability to transfer the sulfane-sulfurs to organic compounds for their stability and storage in biological systems. This study showed that polysulfide detection by L-SERS serves as a potentially useful method applicable to human-derived frozen tissues, and its application to cancer shed light on prediction of the chemoresistance against CDDP in ovarian carcinomas.

Hydropolysulfides can serve as a nucleophile to detoxify electrophiles in biological systems. Recent studies have been focusing on various RSS generated in mammalian cells and tissues. Among them, cysteine hydropersulfide is thought to be a product of CBS or CSE when cystine is used as a substrate for these enzymes [8,22]. While CARS2 has been reported to play a role in the generation of polysulfides [22], other studies have shown that CSE is the major enzyme responsible for polysulfide synthesis [24]. Accumulating evidence suggests that cysteine and glutathione constitute the resources that provide various RSS through by exchanging reducing equivalents with each other; these reactive species consequently form a pool of sulfur atoms in mammals. However, little has been known about how RSS and their parent thiols are regulated and interacted in cancer tissues. Interestingly, the current results obtained from ovarian clear cell carcinoma cell lines suggested that OVTOKO

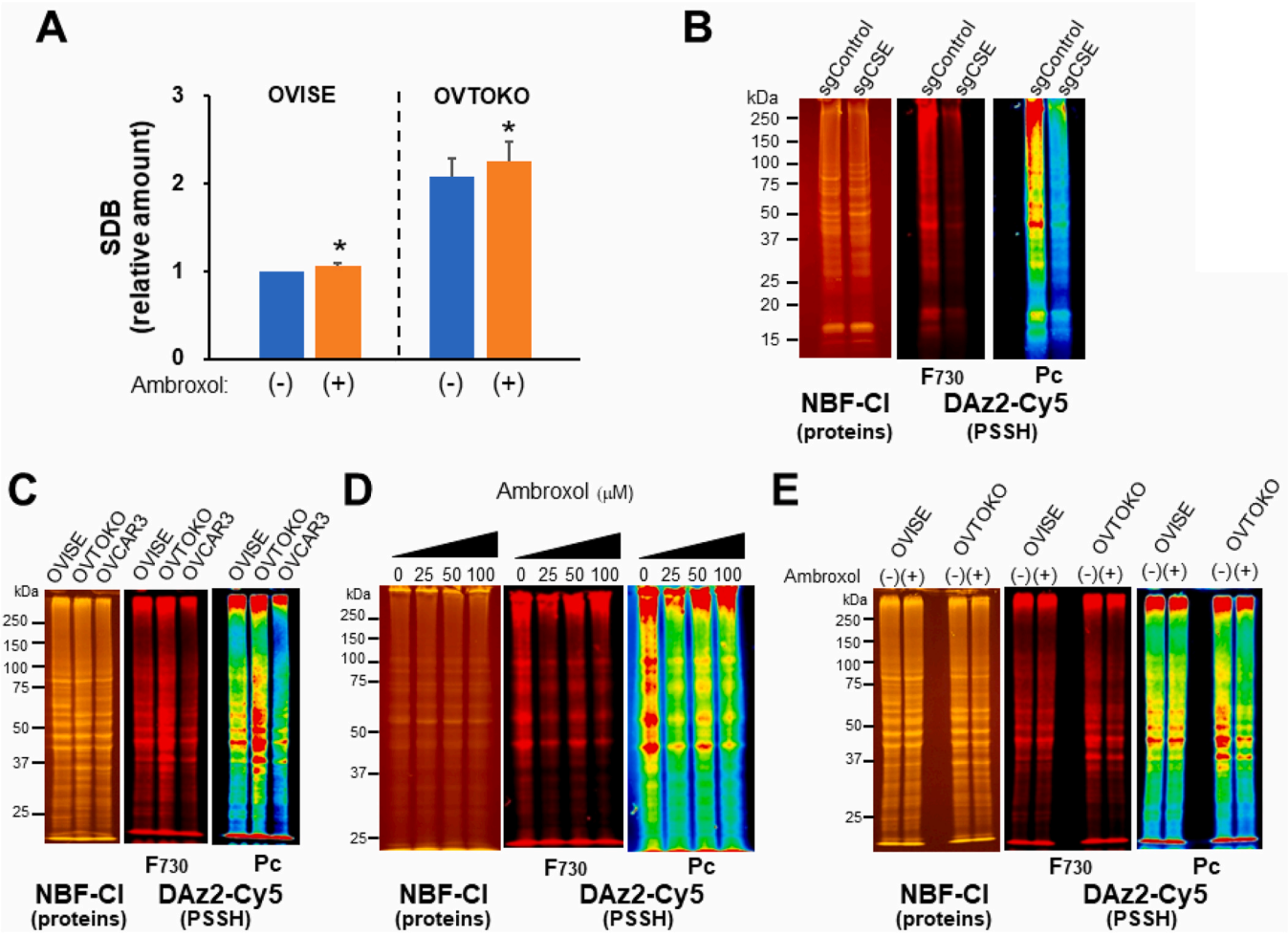

Fig. 7. Alterations in polysulfide and protein persulfide contents in OVISE and OVTOKO cell lines by ambroxol treatment. Panel A: Contents of SDB in OVISE and OVTOKO cells. In these experiments, the presence or absence of ambroxol at 5 mM for 30 min to protein-free cell lysates caused modest but significant increases in SDB in both OVISE and OVTOKO cells. One sample was separated into two to determine SDB in the absence or presence of ambroxol. Mean + SE of 7 separate experiments. *P < 0.05 with paired Student's t-test as compared with the contents in the ambroxol-free control group. Panel B: Effects of ambroxol at given concentrations in the culture medium on protein persulfidation. NBF-CL gel electrophoresis indicates proteins isolated from sgControl- or sgCSE-treated OVISE cells. sgCSE: single strand RNA targeting *CSE* gene. The cells were incubated with ambroxol for 48 h. The DAz2-Cy5 fluorograph of the gel at 730-nm epi-illumination (F_{730}) and the corresponding pseudo-color representation (Pc) were shown to detect protein persulfides (PSSH). Note that CSE knockout by sgCSE abolished PSSH signals. Panel C: Differences in PSSH contents among OVISE, OVTOKO and OVCAR3 cells. Panel D: Incubation of OVISE cells with ambroxol for 48 h, showing remarkable decreases in PSPH signals. Panel E: Effects of direct application of ambroxol at 100 μM directly to the cell lysates of OVISE and OVTOKO cells. Note decreases in PSSH after the ambroxol application in these cells. (For interpretation of the references to color in this figure legend, the reader is referred to the Web version of this article.)

contains highest amounts of SDB and protein persulfides (Figs. 5 and 7), while OVISE exhibits the largest CSE expression. Although mechanisms for such dissociation between the RSS-generating enzyme (CSE and CBS in Fig. 5) remain unknown, recent studies suggest that, among ovarian cancer cell lines, OVTOKO robustly expresses aldehyde dehydrogenase-1 (ALDH1) which decreases electrophilic aldehydes in cancer cells [34,35]: Under these circumstances, net amounts of hydropolysulfides might be apparently increased, because aldehydes counteract nucleophilic hydropolysulfides. Further investigation is necessary to reveal fates of polysulfides and H_2S through non-canonical chemical reactions [36,37].

Our previous studies revealed the potential of imaging metabolomics that combine imaging mass spectrometry with L-SERS technology to determine multiple metabolites including RSS, in cancer [4,24]. To ionize metabolites, imaging MS requires ultraviolet laser irradiation with robust energy that causes artificial oxidation of RSS to yield sulfonated derivatives; imaging of these derivatives provides important but indirect information of RSS distribution of tissues [4,16]. Conversely, L-SERS utilizes infrared laser irradiation that enables the visualization of GSH, hypotaurine, sulfinate, and polysulfides while minimizing the artificial oxidation of these redox metabolites [4]. The current study revealed that CSE is an independent biomarker predicting the prognosis of platinum-based chemotherapy after the debulking surgery of ovarian cancer. To determine metabolites responsible for the chemoresistance, we applied the two different approaches of imaging metabolomics—imaging MS and L-SERS imaging. L-SERS with microscopic pathological annotation enabled the characterization of the spatial heterogeneity of multiple biomarker metabolites in cancer cell nests and the surrounding stromal regions. Observation that polysulfides were significantly greater in both cancer cell nests and stromal regions of CCC versus those of SAC (Fig. 2G and H), while CSE was highly localized in cancer cell nests but not in the surrounding stroma. This observation led us to hypothesize the presence of unidentified molecular mechanisms for polysulfide diffusion and/or shuttling; these mechanisms have yet only been identified in the bacterial kingdom [38]. Assuming such putative diffusion mechanisms and results shown in Fig. 2, distribution of

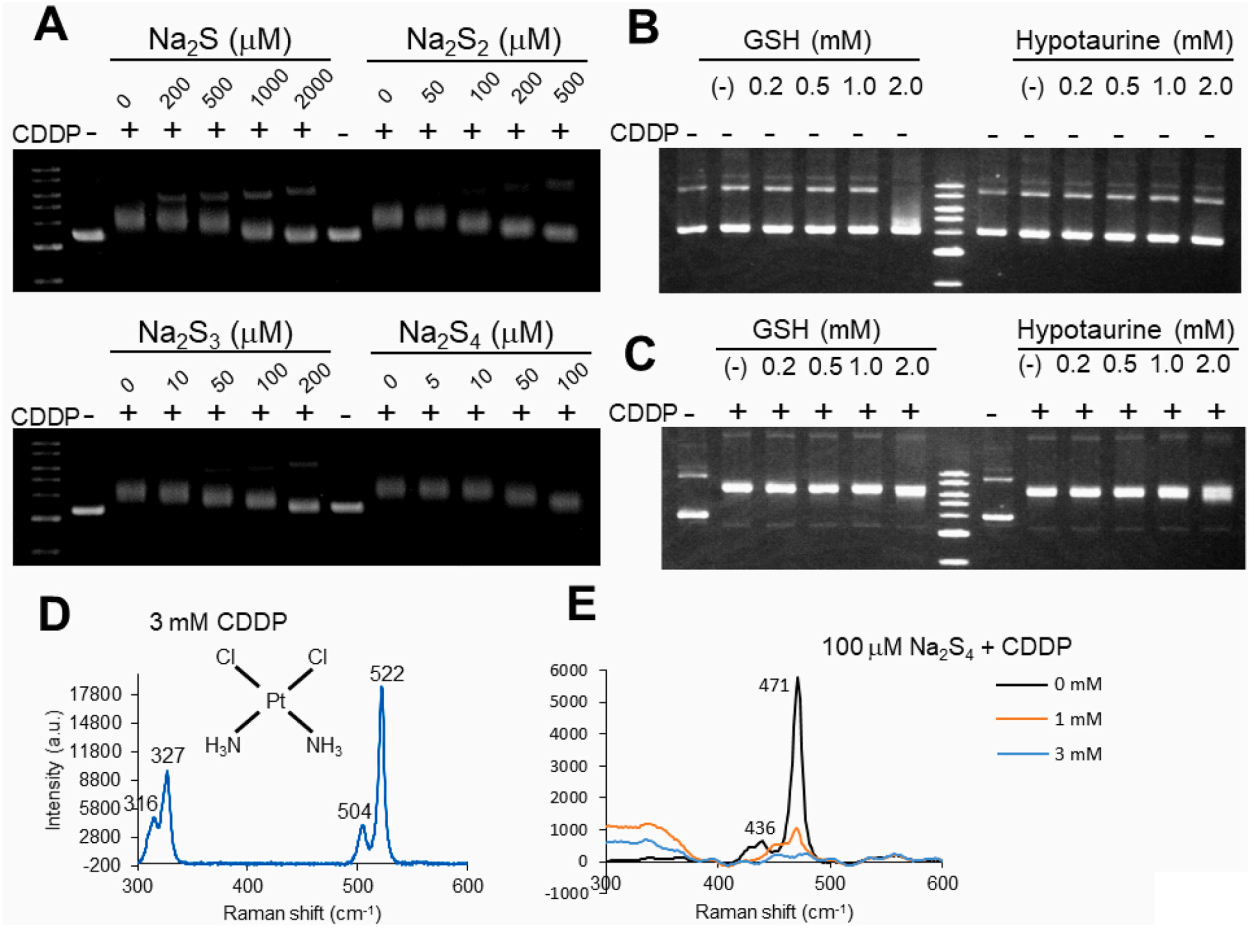

Fig. 8. Disturbance of double-strand DNA supercoiling by CDDP and its attenuation by polysulfides in vitro. Panel A. Gel shift assay of CDDP-induced disturbance of DNA supercoiling and its attenuation by Na_2S, Na_2S_2, Na_2S_3 and Na_2S_4 in vitro. Note that the ability of polysulfides to reverse the CDDP-induced gel shift is dose-dependent and potentiated with increasing number of sulfur atoms. Panels B and C. Effects of GSH and hypotaurine on DNA supercoiling, indicating the absence of effects of GSH or hypotaurine on recovery of DNA supercoiling in the presence of CDDP at 50 μM, respectively. Panel D. A representative Raman spectrum of CDDP at 3 mM. Panel E. Dose-dependent decreases in the peak at 471 cm^{-1} of Na_2S_4 at 100 μmol l^{-1} by adding CDDP at 1 and 3 mM. Measurements in Panels D and E were performed by non-SERS conventional Raman spectroscopy with a grating of 300 grooves/mm.

polysulfides in the CSE-absent stromal regions surrounding the cancer cell nests may serve as a barrier that enables to inactivate CDDP before its access to the core of cancer cell nests.

Among the different RSS, hydropolysulfides, but not GSH or hypotaurine, have a potent inhibitory action on CDDP-induced disturbance of DNA supercoiling (Fig. 8), shedding light on a possibility that polysulfides generated in cancer cell nests and the surrounding stroma in CCC tissues protect against CDDP-induced damages of cancer cells. Roles of cellular glutathione in chemoresistance against CDDP have long been discussed with conflicting results [39,40], raising a question as to whether RSS besides glutathione plays a protective role for cancer cells against CDDP. Among the different ovarian cancer cell lines, OVISE and OVTOKO express greater CSE and generates more endogenous polysulfides than OVCAR-3, a representative of SAC, was chosen to determine whether any reagents that degrade polysulfides render ovarian cancer cells more susceptible to CDDP exposure. The current study revealed that ambroxol, an expectorant for clinical use, enables to degrade polysulfides with its clinically relevant doses and to enhance CDDP-induced OVISE cytotoxicity. While adjuvant effects of ambroxol on anti-cancer reagents have been reported in lung cancer [26,27], the current unexpected result indicating the effects of ambroxol as the polysulfide-degrading reagent shed light on its potential clinical use for future studies. Observation that co-treatment of ambroxol decreased protein persulfidation deserves further studies to identify individual proteins modified by CSE-derived hydropersulfide, providing evidence for roles of functional alterations in target proteins in mechanisms for cancer cell survival.

As shown in Fig. 1B and Fig. 2I–J, the prognosis and CDDP-chemosensitivity of CCC vary robustly among individual patients, and thus pathological diagnosis alone appears insufficient to predict the post-operative overall survival. While future evaluation of SERS imaging by prospective study should be required, the current studies suggest on a possible usefulness of combination of pathological diagnosis with L-SERS technology to determine endogenous polysulfides at the time of surgical operation prior to chemotherapy in ovarian cancer.

Between many SERS devices [41,42], L-SERS is unique in providing pixel-based Raman spectra of many different interatomic vibrational modes in fingerprinting regions over large surface areas of a pathological specimen. Combination with pathological annotation does not only provides evidence for spatial heterogeneity in metabolites in malignancies but also translates into the development of enforced learning for cancer diagnostics [4]. In CCC, polysulfides occur in not only cancer cell nests but also the surrounding stroma. The limitation of our study is that we could not specify the discernible molecular entities of endogenous polysulfides that are responsible for the signal at 480 cm^{-1}. As reported previously [4], this technology can hardly capture protein-bound polysulfides hidden in the milieu interieur, because the distance between adjacent Au nanoparticles is too small to allow proteins to access hot spots of the near field light. In this study, oxidized glutathione trisulfide generated little sulfane-sulfur signals (Fig. 3C), suggesting that L-SERS

enables to detect inorganic or low-molecular organic polysulfides, but not those with greater molecular weights or those bound to the surface of proteins. With greater spatial resolution and SERS knowledgebase of the fingerprinting regions at the molecular basis, further studies on the methodology are required to reveal mechanisms underlying the metabolic interplays between cancer and stromal cells. L-SERS imaging does not require any staining and molecular labelling on tissues, and its translational refinement deserves further studies to be brushed up as a comprehensive device and to support the pathological diagnosis of intractable drug-resistant cancers.

Funding

This work was supported by Japan Agency for Medical Research and Development (AMED) which included a grant of JP201m0203004 (T. H.), AMED-CREST for Metabolism (K.H. and Y.K.). The study was also supported by a Grant-in-Aid for Scientific Research (B), and a Challenging Exploratory Research grant from the Ministry of Education, Culture, Sports, Science and Technology (MEXT) of Japan (K.H.). Research Foundation for Opto-Science and Technology in Hamamatsu-City (T.Y.) supports funding for cell biology experiments. Infrastructure for metabolomics and Raman spectroscopy to determine persulfides was supported by JST ERATO Suematsu Gas Biology Project (M.S.) until March 2015. Infrastructure of laser-scanning confocal Raman spectroscopy was supported by AMED-CREST (Y.K. JP17gm0710010) and partly by JST Moonshot Program for Cancer Research from 2020.

CRediT authorship contribution statement

Kazufumi Honda: Data curation, Formal analysis, contributed to fundamental design and data analyses and protocols, is responsible for checking a quality of clinical data analyses. **Takako Hishiki:** Data curation, Formal analysis, contributed to fundamental design and data analyses and protocols. **Sohei Yamamoto:** Data curation, Formal analysis, contributed to fundamental design and data analyses and protocols. **Takehiro Yamamoto:** contributed to experiments of cell biology and pharmacology. **Nami Miura:** contributed to experiments of cell biology and pharmacology. **Akiko Kubo:** collected all data of imaging MS. **Mai Itoh:** Data curation, Formal analysis. **Wei-Yu Chen:** worked for data analyses of NDMC cohorts. **Masashi Takano:** worked for data analyses of NDMC cohort. **Tomoyuki Yoshikawa:** Data curation, Formal analysis. **Takahiro Kasamatsu:** Data curation, Formal analysis. **Shinichiro Sonoda:** Data curation, Formal analysis. **Hirotoshi Yoshizawa:** Data curation, Formal analysis. **Seigo Nakamura:** Data curation, Formal analysis. **Yuichiro Itai:** Data curation, Formal analysis. **Megumi Shiota:** set up the infrastructure of laser scanning Raman spectroscopy. **Daisuke Koike:** Data curation, Formal analysis. **Masayuki Naya:** Data curation, Formal analysis. **Noriyo Hayakawa:** Data curation, Formal analysis. **Yoshiko Naito:** Data curation, Formal analysis. **Tomomi Matsuura:** Data curation, Formal analysis. **Keiko Iwaisako:** Data curation, Formal analysis. **Toshihiko Masui:** Data curation, Formal analysis. **Shinji Uemoto:** contributed to data analyses. **Kengo Nagashima:** worked for quality control of statistical analyses. **Yoshinori Hashimoto:** Data curation, Formal analysis. **Tomohiro Sakuma:** Data curation, Formal analysis. **Osamu Matsubara:** Data curation, Formal analysis. **Wilber Huang:** Data curation, Formal analysis. **Tomoaki Ida:** contributed to chemical synthesis of standard compounds. **Takaaki Akaike:** contributed to chemical synthesis of standard compounds. **Yohei Masugi:** Data curation, Formal analysis. **Michiie Sakamoto:** Data curation, Formal analysis. **Tomoyasu Kato:** Data curation, Formal analysis. **Yoshinori Ino:** Data curation, Formal analysis. **Hiroshi Yoshida:** Data curation, Formal analysis. **Hitoshi Tsuda:** Data curation, Formal analysis. **Nobuyoshi Hiraoka:** Data curation, Formal analysis. **Yasuaki Kabe:** Data curation, Formal analysis. **Makoto Suematsu:** Data curation, Formal analyses, contributed to fundamental design and data analyses and protocols, is responsible for checking a quality of experimental data of on-tissue SERS imaging and cell biology.

Declaration of competing interest

The authors have no competing interests to declare.

Acknowledgements

This work was supported by AMED-CREST (Y.K. and K.H.), a Grant-in Aid for Scientific Research (B), and a Challenging Exploratory Research grant from the Ministry of Education, Culture, Sports, Science and Technology (MEXT) of Japan (K.H.). The study of cell biology in vitro besides clinical researches was supported by Research Foundation for Opto-Science and Technology in Hamamatsu-City, Japan (T.Y.). Infrastructure of imaging MS was developed by JST ERATO Suematsu Gas Biology (2010–2015 led by M.Su.). Laser-confocal line scanning SERS was supported by AMED-CREST (led by Y.K.). The study sponsors played no role in the study design, in the collection, analysis or interpretation of data, in the writing of the manuscript, or in the decision to submit the manuscript for publication. All authors confirm that they have reviewed and agreed to the submission of this manuscript.

Appendix A. Supplementary data

Supplementary data to this article can be found online at https://doi.org/10.1016/j.redox.2021.101926.

References

[1] M.E. van der Burg, M. van Lent, M. Buyse, A. Kobierska, N. Colombo, G. Favalli, A. J. Lacave, N. Nardi, J. Renard, S. Pecorelli, The effect of debulking surgery after induction chemotherapy on the prognosis in advanced epithelial ovarian cancer. Gynecological Cancer Cooperative Group of the European Organization for Research and Treatment of Cancer, N. Engl. J. Med. 332 (10) (1995) 629–634.

[2] H. Yamada, N. Akahoshi, S. Kamata, Y. Hagiya, T. Hishiki, Y. Nagahata, T. Matsuura, N. Takano, M. Mori, Y. Ishizaka, T. Izumi, Y. Kumagai, T.T. Kasahara, M. Suematsu, I. Ishii, Methionine excess in diet induces acute lethal hepatitis in mice lacking cystathionine γ-lyase, an animal model of cystathioninuria, Free Radic. Biol. Med. 52 (9) (2012) 1716–1726.

[3] T. Chiku, D. Padovani, W. Zhu, S. Singh, V. Vitvisky, R. Banerjee, H_2S biogenesis by human cystathionine gamma-lyase leads to the novel sulfur metabolites lanthionine and homolanthionine and is responsive to the grade of hyperhomocysteinemia, J. Biol. Chem. 284 (17) (2009) 11601–11612.

[4] M. Shiota, M. Naya, T. Yamamoto, T. Hishiki, T. Tani, H. Takahashi, A. Kubo, D. Koike, M. Itoh, M. Ohmura, Y. Kabe, Y. Sugiura, N. Hiraoka, T. Morikawa, K. Takubo, K. Suina, H. Nagashima, O. Sampetrean, O. Nagano, H. Saya, S. Yamazoe, H. Watanabe, M. Suematsu, Gold-nanofève surface-enhanced Raman spectroscopy visualizes hypotaurine as a robust anti-oxidant consumed in cancer survival, Nat. Commun. 9 (1) (2018) 1561.

[5] L. Li, P. Rose, P.K. Moore, Hydrogen sulfide and cell signaling, Annu. Rev. Pharmacol. Toxicol. 51 (2011) 169–187.

[6] N. Lau, M.D. Pluth, Preactive sulfur species (RSS): persulfides, polysulfides, potential, and problems, Curr. Opin. Chem. Biol. 49 (2019) 1–8.

[7] T. Morikawa, K. Kajimura, T. Nakamura, T. Hishiki, T. Nakanishi, Y. Yukutake, Y. Nagahata, M. Ishikawa, K. Hattori, T. Takenouchi, T. Takahashi, I. Ishii, K. Matsubara, Y. Kabe, S. Uchiyama, E. Nagata, M.M. Gadalla, S.H. Snyder, M. Suematsu, Hypoxic regulation of the cerebral microcirculation is mediated by a carbon monoxide-sensitive hydrogen sulfide pathway, Proc. Natl. Acad. Sci. U.S.A. 109 (4) (2012) 1293–1298.

[8] T. Ida, T. Sawa, H. Ihara, Y. Tsuchiya, Y. Watanabe, Y. Kumagai, M. Suematsu, H. Motohashi, S. Fujii, T. Matsunaga, M. Yamamoto, K. Ono, N.O. Devarie-Baez, M. Xian, J.O. Fukuto, T. Akaike, Reactive cysteine persulfides and S-polythiolation regulate oxidative stress and redox signaling, Proc. Natl. Acad. Sci. U.S.A. 111 (21) (2014) 7606–7611.

[9] Y. Shimizu, S. Kamoi, S. Amada, F. Akiyama, S.G. Silverberg, Toward the development of a universal grading system for ovarian epithelial carcinoma: testing of a proposed system in a series of 461 patients with uniform treatment and follow-up, Cancer 82 (5) (1998) 893–901.

[10] S.G. Silverberg, Histopathologic grading of ovarian carcinoma: a review and proposal, Int. Soc. Gynecol. Pathol. 19 (1) (2000) 7–15.

[11] S. Yamamoto, H. Tsuda, K. Honda, T. Kita, M. Takano, S. Tamai, J. Inazawa, T. Yamada, O. Matsubara, Actinin-4 expression in ovarian cancer: a novel prognostic indicator independent of clinical stage and histological type, Mod. Pathol. 20 (12) (2007) 1278–1285.

[12] E.A. Eisenhauer, P. Therassel, J. Bogaerts, L.H. Schwartz, D. Sargent, R. Ford, J. Dancy, S. Arbuck, S. Gwyther, M. Mooney, L. Rubinstein, L. Shankar, L. Dodd, R. Kaplan, D. Lacombe, J. Verweij, New response evaluation criteria in solid

tumours: revised RECIST guideline (version 1.1), Eur. J. Canc. 45 (2) (2009) 228–247.
[13] K. Honda, M. Kobayashi, T. Okusaka, J.A. Rinaudo, Y. Huang, T. Marsh, M. Sanada, Y. Sasajima, S. Nakamori, M. Shimahara, T. Ueno, A. Tsuchida, N. Sata, T. Ioka, Y. Yasunami, T. Kosuge, N. Miura, M. Kamita, T. Sakamoto, H. Shoji, G. Jung, S. Srivastava, T. Yamada, Plasma biomarker for detection of early stage pancreatic cancer and risk factors for pancreatic malignancy using antibodies for apolipoprotein-AII isoforms, Sci. Rep. 5 (2015) 15921.
[14] Y. Benjamini, Y. Hochberg, Controlling the false discovery rate: a practical and powerful approach to multiple testing, J. Roy Statist. Soc. Ser. B57 (1995) 289–300.
[15] S. Yamazoe, M. Naya, M. Shiota, T. Morikawa, A. Kubo, T. Tani, T. Hishiki, T. Horiuchi, M. Suematsu, M. Kajimura, Large-area surface-enhanced Raman spectroscopy imaging of brain ischemia by gold nanoparticles grown on random nanoarrays of transparent boehmite, ACS Nano 8 (6) (2014) 5622–5632.
[16] T. Yamamoto, N. Takano, K. Ishiwata, M. Ohmura, Y. Nagahata, T. Matsuura, A. Kamata, K. Sakamoto, T. Nakanishi, A. Kubo, T. Hishiki, M. Suematsu, Reduced methylation of PFKFB3 in cancer cells shunts glucose towards the pentose phosphate pathway, Nat. Commun. 5 (2014) 3480.
[17] Y. Kabe, T. Nakane, I. Koike, T. Yamamoto, Y. Sugiura, E. Harada, K. Sugase, T. Shimamura, M. Ohmura, K. Muraoka, A. Yamamoto, T. Uchida, S. Iwata, Y. Yamaguchi, E. Krayukhina, M. Noda, H. Handa H, K. Ishimori, S. Uchiyama, T. Kobayashi, M. Suematsu, Haem-dependent dimerization of PGRMC1/sigma-2 receptor facilitates cancer proliferation and chemoresistance, Nat. Commun. 7 (2016) 11030.
[18] M. Jinek, K. Chylinski, I. Fonfara, M. Hauer, J.A. Doudna, E. Charpentier, A programmable dual-RNA-guided DNA endonuclease in adaptive bacterial immunity 337 (2012) 816–821.
[19] H.A. Hamid, A. Tanaka, T. Ida, A. Nishimura, T. Matsunaga, S. Fujii, M. Morita, T. Sawa, J.M. Fukuto, P. Nagy, R. Tsutsumi, H. Motohashi, H. Ihara, T. Akaike, Polysulfide stabilization by tyrosine and hydroxyphenyl-containing derivatives that is important for reactive sulfur metabolomics analysis, Redox Biol. 21 (2019) 101096.
[20] J. Zivanovic, E. Kouroussis, J.B. Kohl, B. Adhikari, B. Bursac, S. Schott-Roux, D. Petrovic, J.L. Miljkovic, D. Thomas-Lopez, Y. Jung, M. Miler, S. Mitchell, V. Milosevic, J.E. Gomes, M. Benhar, B. Gonzalez-Zom, I. Ivanovic-Burmazovic, R. Torregrossa, J.R. Mitchell, M. Whiteman, G. Schwarz, S.H. Snyder, B.D. Paul, K. S. Carrol, M.R. Filipovic, Selective persulfide detection reveals evolutionally conserved antiaging effects of S-sulfidation, Cell Metabol. 30 (2019) 1152–1170. e13.
[21] M.J. de Miguel-Luken, M. Chaves-Conde, B. Quintana, A.N. Menoyo, I. Torado, V. Miguel-Luken, J. Pachon, D. Chinchon, V. Suarez, A. Carnero, Phosphorylation of gH2AX as a novel prognostic biomarker for laryngoesophageal dysfunction-free survival, Oncotarget 7 (22) (2016) 31723–31727.
[22] E. Takatori, T. Shoji, S. Kumagai, T. Sawai, A. Kurose, T. Sugiyama, Are platinum agents, paclitaxel and irinotecan effective for clear cell carcinoma of the ovary? : DNA damage detected with gH2AX induced by anticancer agents, J. Ovarian Res. 5 (2012) 16.
[23] K. Honda, M. Ono, M. Shitashige, M. Masuda, M. Kamita, N. Miura, T. Yamada, Proteomic approaches to the discovery of cancer biomarkers for early detection and personalized medicine, Jpn. J. Clin. Oncol. 43 (2) (2013) 103–109.
[24] S.-I. Bibli, B. Luck, S. Zukunft, J. Witting, W. Chen, M. Xian, A. Papapetropoulos, J. Hu, I. Fleming, A selective and sensitive method for quantification of endogenous polysulfide production in biological samples, Redox Biol. 18 (2018) 295–304.
[25] T. Akaike, T. Ida, F.Y. Wei, M. Nishida, Y. Kumagai, M.M. Alam, H. Ihara, T. Sawa, T. Matsunaga, S. Kasamatsu, A. Nishimura, M. Morita, K. Tomozawa, A. Nishimura, S. Watanabe, K. Inabe, H. Shima, N. Tanuma, M. Jung, S. Fujii, Y. Watanabe, M. Ohmuraya, P. Nagy, M. Feelisch, J.M. Fukuto, H. Motohashi, Cysteinyl-tRNA synthetase governs cysteine polysulfidation and mitochondrial bioenergetics, Nat. Commun. 8 (2017) 1177.
[26] X. Zhang, Q. Chen, M. Chen, Z. Ren, X. Wang, Q.J. Qian, Y. Sunm, Z. Sha, Ambroxol enhances anti-cancer effect of microtubule-stabilizing drug to lung carcinoma through blocking autophagic flux in lysosome-dependent way, Am. J. Canc. Res. 7 (12) (2017) 2406–2421.
[27] X. Wang, L. Wang, H. Wang, H. Zhang, Perioperative lung cancer protection provided by high-dose ambroxol in patients with lung cancer, Cell Biochem. Biophys. 73 (2015) 281–284.
[28] A.M.F. Shayea, A.M.A. Mousa, W.M. Renno, M.S. Nadar, B. Qabazard, M.H. M. Yousif, Chronic treatment with hydrogen sulfide donor GYY4137 mitigates microglial and astrocyte activation in the spinal cord of streptozotocin-induced diabetic rats, J. Neuropathol. Exp. Neurol. 79 (2) (2020) 1320–1343.
[29] S. Zorbas-Seifried, C.G. Hartinger, K. Meelich, M. Galanski, B.K. Keppler, H. Zorbas, DNA interactions of pH-sensitive, antitumor bis(aminoalcol) dichloroplatinum(II) complexes, Biochemistry 45 (2006) 14817–14825.
[30] H.-K. Liu, P.J. Sadler, Metal complexes as DNA intercalators, Acc. Chem. Res. 44 (5) (2011) 349–359.
[31] M. Mardamshina, T. Geiger, Next-generation proteomics and its application to clinical breast cancer research, Am. J. Pathol. 187 (2017) 2175–2184.
[32] H. Kimura, Signaling of hydrogen sulfide and polysulfides, Antioxidants Redox Signal. 22 (5) (2015) 347–349.
[33] Y. Kimura, Y. Toyofuku, S. Koike, N. Shibuya, N. Nagahara, D. Lefer, Y. Ogasawara, H. Kimura, Identification of H_2S_3 and H_2S produced by 3-mercaptopyruvate sulfurtransferase in the brain, Sci. Rep. 5 (2015) 14774.
[34] T. Mizuno, N. Suzuki, H. Makino, T. Furui, E. Mori, H. Aoki, T. Kunisada, M. Yano, S. Kuji, Y. Hirashima, A. Arakawa, S. Nishio, K. Ushijima, Y. Itani, K. Morishige, Cancer stem cell-like cells of ovarian clear cell carcinoma are enriched in the ALDH-high population associated with an accelerated scanvenging system in reactive oxygen species, Gynecol. Oncol. 137 (2015) 299–305.
[35] M. Suematsu, Can drug repurposing stop “chase and run” between aldehydes and reactive sulfur species in anti-cancer therapy? Oncotarget 9 (77) (2018) 34453–34454.
[36] K.R. Olson, Y. Gao, F. Arif, K. Aroma, S. Patel, E.R. DeLeon, T.R. Sutton, M. Feelisch, M.M. Cortese-Krott, K.D. Staub, Metabolism of hydrogen sulfide (H_2S) and production of reactive sulfur species by superoxide dismutase, Redox Biol. 15 (2018) 74–85.
[37] V. Vitvitsky, P.K. Yadav, A. Kurthen, R. Banerjee, Sulfide oxidation by a noncanonical pathway in red blood cells generates thiosulfate and polysulfides, J. Biol. Chem. 290 (13) (2015) 8310–8320.
[38] S. Riedel, B. Siemiatkowska, M. Watanabe, C.S. Muller, V. Schnemann, R. Hoefgen, S. Leimkuhler, The ABCB7-like transporter PexA in Rhodobacter capsulatus is involved in the translocation of reactive sulfur species, Front. Microbiol. 10 (2019) 406.
[39] Z.G. Zheng, H. Xu, S.S. Suo, X.L. Xu, M.W. Ni, L.H. Gu, W. Chen, L.Y. Wang, Y. Zhao, B. Tian, Y.J. Hua, The essential role of H19 contributing to cisplatin resistance by regulating glutathione metabolism in high-grade serous ovarian cancer, Sci. Rep. 19 (6) (2016) 26093.
[40] N. Nikounezhad, M. Nakhjavani, F.H. Shirazi, Cellular glutathione level does not predict ovarian cancer cells’ resistance after initial or repeated exposure to cisplatin, J. Exp. Therapeut. Oncol. 12 (1) (2017) 1–7.
[41] S. Laing, L.E. Jamieson, K. Faulds, D. Graham, Surface-enhanced Raman spectroscopy for in vivo biosensing, Nat. Rev. Chem. 1 (2017) 1–19.
[42] J. Wang, K.M. Koo, Y. Wang, M. Trau, Engineering state-of-the-art plasmonic nanomaterials for SERS-based clinical liquid biopsy applications, Adv. Sci. 6 (23) (2019) 1900730.